الجـــــــــــــــــــــــمـهـوريـــــة الجــــــــــــــــــزائـريـة الديمـــــــقـراطيـة الـشــــــــــعبيـة

People's Democratic Republic of Algeria

وزارة التـــــــــــــــــــــــــــــــــعـليـم العـــــــالي و البـــــــــــــحث العـــلـمـــي

Ministry of Higher Education and Scientific Research

جـــــــــــــــــامعة أبي بـكـــر بـلـقــايـد – تــلمســــــــــــــــــان –

Univrsity of Aboubakr Belkaïd – Tlemcen –

Faculty of TECHNOLOGY

THESIS

presented for obtaining the **Master's degree**

In: Mechanical engineering

Specialty: Energetics

By: Ibrahim Sadi Ibrahim Solimieh and Mohammed Iyad Zead Elmadhoon

Subject

3D Numerical and Experimental Study of Double Pass Solar Air Collector

Publicly defended / /, In front of the jury composed of

Mr/ Saim Rachid	Pr	University of Tlemcen	President
Mme / Sari Hassoun Hind	MAA	University of Tlemcen	Examiner
Mr/ Guellil Hocine	MCA	University of Tlemcen	Supervisor
Mr/ Korti Nabil Abdelillah	Pr	University of Tlemcen	Co-supervisor

Academic year: 2023/2024

THANKS

Praise be to Allah, the Lord of all worlds, who has granted us the ability to complete this work and for all the blessings we enjoy by His grace.

We extend our deepest thanks and appreciation to Mr. Korti Nabil Abdelillah for his time and dedicated efforts in helping us complete this work. His guidance and support have been invaluable.

We also sincerely thank Mr. Guellil Hocine for his significant contributions and unwavering support throughout this project.

Our gratitude also extends to Mr. Noureddine Embarek for his assistance and efforts.

Special recognition goes to the committee members, Mr. Saim Rachid and Mme. Sari Hassoun Hind, for their thorough evaluation and kind presence at our presentation.

Lastly, we extend our gratitude to the entire university staff for their dedication to academic excellence and student support. Your commitment and passion for education have created an environment where students can excel and achieve their full potential.

DEDICATION

To my family,

With deepest gratitude, this thesis is dedicated to you, the foundation of my life and the stars in my sky. To my parents, your sacrifices have paved the way for my dreams, and your wisdom and love have guided me through every challenge. You have instilled in me the courage to aspire and the strength to achieve.

To my siblings, whose boundless support and infectious laughter have lightened the heaviest days and brightened the darkest nights. Your unwavering belief in me has been a beacon of hope.

This achievement is a reflection of my efforts and a testament to your unconditional love and support. To you, I owe all that I am and all that I strive to be.

With all the love in my heart,

Ibrahim and Mohammed

Abstract

This study investigates the effect of changing the gap (distance) between the absorber plate and the glass cover of a double-pass solar air collector (DPSAC) on its thermal efficiency(η_{th}) and dynamic behavior. An experimental study was conducted using gaps of 3 cm, 6 cm, 9 cm, and 12 cm, with a solar radiation (I) of 270 W/m². The primary focus was on evaluating how the gap distance influences the collector's ability to convert solar energy into usable thermal energy. The thermal performance was further assessed using a three-dimensional (3D) Computational Fluid Dynamics (CFD) simulation in ANSYS Fluent.

The results of the experimental and numerical studies were validated by comparing them, revealing nuanced insights into the thermal and dynamic behavior of the collector that could not be fully captured through experimentation alone. Specifically, the thermal efficiency was found to reach its maximum at 68.91% with a 12 cm gap and its minimum at 52.63% with a 3 cm gap. Additionally, the maximum temperature difference was observed with the 3 cm gap at 19.36°C, while the minimum temperature difference was observed with the 12 cm gap at 17.18°C.

Keywords: DPSAC, Gap, Thermal efficiency, CFD simulation, ANSYS Fluent, Dynamic behavior, thermal behavior.

الملخص

تبحث هذه الدراسة في تاثير تغيير المسافة بين لوح الامتصاص والغطاء الزجاجي لجامع هواء شمسي مزدوج المسار على كفائته الحرارية وسلوكه الديناميكي, تم اجراء دراسة تجريبية باستخدام فجوات قدرها 3 سم, 6 سم, 9 سم و 12 سم مع اشعاع شمسي قدرته 270 واط/متر مربع, كان التركيز الرئيسي على تقييم كيفية تأثير مسافة الفجوة على قدرة الجامع على تحويل الطاقة الشمسية إلى طاقة حرارية قابلة للاستخدام, تم تحليل الكفائة الحرارية للجامع بشكل اعمق باستخدام حوسبة الموائع الديناميكية ثلاثية الابعاد بواسطة برنامج انسيس فليينت.

تم التحقق من النتائج الرقمية بمقارنتها مع النتائج التجريبية, مما ادى الى امتلاك نظرة شمولية على السلوك الديناميكي والسلوك الحراري للجامع, الذي لا يمكن فهمه جيدا من خلال التجربة وحدها. وتحديدًا، وجد أن الكفاءة الحرارية بلغت أقصى معدل لها عند 68.91% مع فجوة 12 سم وأدنى معدل عند 52.63% مع فجوة 3 سم. بالإضافة إلى ذلك، تم ملاحظة أقصى فارق حراري مع الفجوة 3 سم بلغ 19.36 درجة مئوية، في حين تم ملاحظة أدنى فارق حراري مع الفجوة 12 سم بلغ 17.18 درجة مئوي.

كلمات مفتاحية: جامع هواء شمسي مزدوج المسار, الفجوة, الكفائة الحرارية, حوسبة الموائع الديناميكية, انسيس فليينت, السلوك الديناميكي, السلوك الحراري.

Résumé

Cette étude examine l'effet de la variation de l'écart (distance) entre la plaque absorbeuse et la couverture en verre d'un collecteur solaire d'air à double passage (DPSAC) sur son efficacité thermique (η_{th}) et son comportement dynamique. Une étude expérimentale a été réalisée en utilisant des écarts de 3 cm, 6 cm, 9 cm et 12 cm, avec un rayonnement solaire (I) de 270 W/m². L'accent principal était mis sur l'évaluation de l'influence de la distance entre les écarts sur la capacité du collecteur à convertir l'énergie solaire en énergie thermique utilisable. Les performances thermiques ont été évaluées en utilisant une simulation de dynamique des fluides computationnelle tridimensionnelle (CFD) dans ANSYS Fluent.

Les résultats des études expérimentales et numériques ont été validés en les comparant, révélant des insights nuancés sur le comportement thermique et dynamique du collecteur qui ne pourraient pas être pleinement capturés par l'expérimentation seule. Plus précisément, il a été constaté que l'efficacité thermique atteignait son maximum à 68,91 % avec un écart de 12 cm et son minimum à 52,63 % avec un écart de 3 cm. De plus, la différence de température maximale a été observée avec l'écart de 3 cm à 19,36 °C, tandis que la différence de température minimale a été observée avec l'écart de 12 cm à 17,18 °C.

Mots-clés : DPSAC, Écart, Efficacité thermique, Simulation CFD, ANSYS Fluent, Comportement dynamique, Comportement thermique.

Contents

List of Figures

List of Tables

Nomenclature

A_{abs}	Absorber surface area	$[m^2]$
θ	Angle	$[°]$
h	Convective heat transfer coefficient	$[W/m^2K]$
x, y, z	direction	
Gr	Grashof number	
D_h	Hydraulic number	$[m]$
L	length	$[m]$
$\dot{m}$	Mass flow rate	$[kg/s]$
Nu	Nusselt number	
q_{rad}	Net Radiative Heat Flux	$[W/m^2]$
j	Radiosity	
Ra	Rayleigh number	
σ	Stefan-Boltzmann constant (5.67×10^{-8})	$[W/m^2K^4]$
I		
T	Temperature	$[°C]$
ΔT	Temperature difference	$[°C]$
V	velocity	$[m/s]$
W	width	$[m]$

Greek letters

α_a	Absorber plate absorptivity	
ρ	Density	$[kg/m^3]$
α_g	Glass absorptivity	
τ_g	Glass transmissivity	
ε_g	Glass emissivity	

η_{th}	Thermal efficiency	
λ	Thermal conductivity	$[W / mK]$
Cp	Specific heat	$[J / kgK]$
μ	viscosity	$[kg / m\ s]$

Subscripts

a	air
i	ambient
Abs	absorber
EXP	experimental
g	glass
min	minute
NUM	numerical
out	outlet

Abbreviations

CFD	Computational fluid dynamics
MFR	Mass flow rate
SAH	Solar air heater
ARE	Average relative error
CV	Control volume
DPSAC	Double pass solar air collector
DPSAH	Double pass solar air heater
DC	Direct current
FVM	Finite volume method
S2S	Surface to surface
SC	Solar collector
SAC	Solar air collector
SPSAC	Single pass solar air collector

General Introduction

General Introduction

In recent years, the critical role of renewable energy sources has been underscored by factors such as the global oil crisis, escalating energy demands, sustainable availability, and their reduced impact on environmental and public health [1]. Among the wide range of solar thermal technologies, solar water heaters, and solar air collectors stand out due to their simple design and notable thermal efficiency. Solar air collectors, particularly, are extensively employed in drying processes because of their operational simplicity and economic efficiency [2]. Despite the inherently lower efficiency of solar air collectors, reflecting from the minimal thermal capacity of air and inefficient heat transfer rates between the collector surfaces and air, they present numerous benefits. These benefits include immunity to freezing and pressure-related failures, affordability in terms of construction and maintenance, and the elimination of heat exchangers for direct space heating applications [3].

There are principally two configurations of solar air collectors: Single Pass Solar Air Collectors (SPSACs) and Double Pass Solar Air Collectors (DPSACs). In SPSACs, the air is channeled once through the collector, which absorbs solar energy and heats up, subsequently directed towards heating applications. DPSACs, however, incorporate a more complex arrangement whereby air traverses the absorber twice, considerably enhancing the heat transfer efficiency [4]. Research indicates that advancements in DPSAC design can result in 10–15% thermal efficiency gains over SPSACs, confirming their enhanced performance capabilities [5].

Two critical factors in our research are simplicity and cost-effectiveness. The novelty of our study lies in its focus on the position of the absorber, precisely the gap between the absorber and the glass cover. We conducted tests with four different configurations—3 cm, 6 cm, 9 cm, and 12 cm—to determine the optimal configuration using experimental methods and computational fluid dynamics (CFD) simulations. This approach provides new insights into optimizing absorber placement for enhanced thermal performance.

Our thesis is divided into four chapters. The first chapter discusses the literature review, focusing on recent research advancements in double-pass solar air collectors. The second chapter details the experimental procedures, including the design and prototyping of the collector. The third chapter describes the process of simulating the collector using CFD conducted using ANSYS Fluent. The fourth chapter presents all the results, both experimental and numerical.

Chapter 1: Literature Review

Literature Review

Solar thermal devices, such as solar water heaters and collectors (SCs), are renowned for their simple designs and impressive thermal efficiency. SCs offer an economical and user-friendly solution that is extensively used in diverse applications such as drying and space heating. These systems function by utilizing the fundamental idea of using solar energy to elevate the air temperature [2]. The increase in temperature is accomplished by directing air over a surface that absorbs solar radiation, enabling the air to take up thermal energy. Therefore, solar air collectors SACs effectively use renewable energy for various heating requirements. Single-Pass Solar Air Collectors SPSACs and Double-Pass Solar Air Collectors (DPSACs) are two distinct categories of solar thermal collectors. In SPSAC, air flows through the collector only once and is heated by solar radiation before being used for heating. DPSACs, in contrast, include an intricate design where air enters, traverses the absorber twice, and then departs. DPSACs, with their enhanced heat transfer efficiency, offer a fascinating advantage over SPSACs. The double-pass design facilitates prolonged interaction between the air and the absorber surface, leading to improved thermal efficiency and increased solar energy utilization, as shown in Figure 1.1, Wooden frame (1), Upper inlet port (2), Lower inlet port (3), Glass cover (4), Absorber plate (5), Outlet port (6), Insulated tube (7), Blower (8), Metal stand (10), [4].

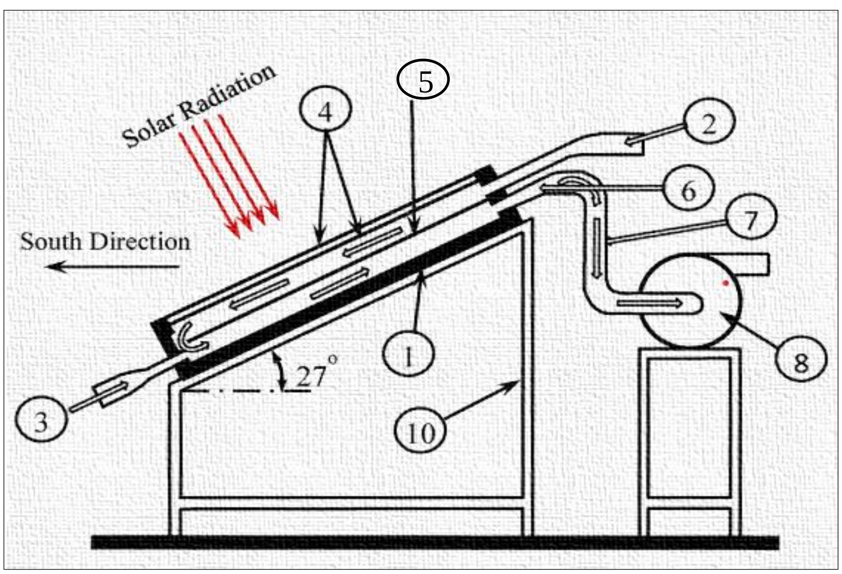

Fig.1.1. The experimental setup of DPSAC [4].

1.1. Influence of Flow Rates and Fin Configurations on DPSAC

Exploration of thermal dynamics in DPSAC by Akrout et al [6]. highlights the impact of parallel, vertical, and opposite fin configurations as shown in Figure 1.2; using Computational Fluid Dynamics (CFD), thermal and velocity profiles are analyzed across varying mass flow rates (MFR) from 0.0036 kg/s to 0.0183 kg/s. Results reveal that parallel fins enhance thermal efficiency, particularly at lower flow rates, while vertical and opposite fins cause increased pressure without a corresponding temperature rise. This finding underscores the importance of incorporating parallel fins in future solar air collector designs to optimize performance, especially at lower flow rates, enhancing solar heating systems' overall efficiency from theoretical and applied perspectives.

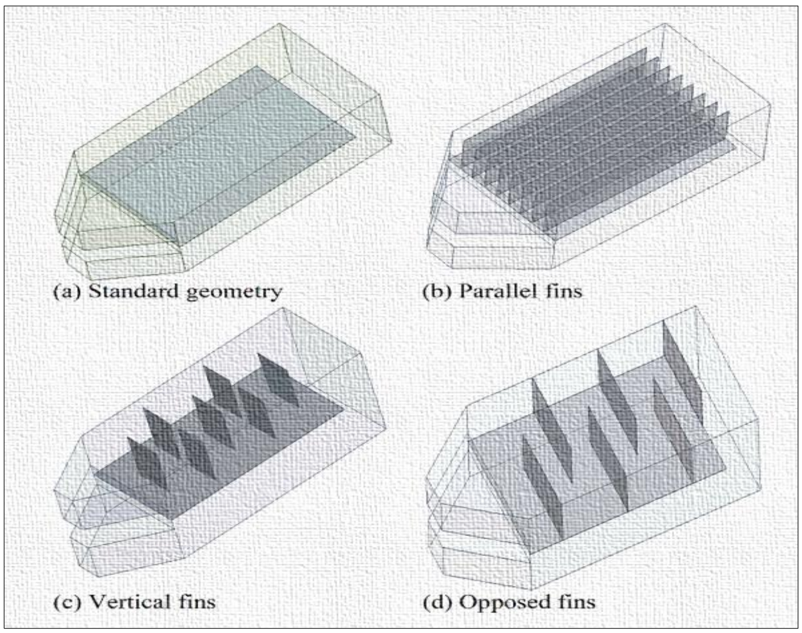

Fig.1.2. Comparative visualisation of different fin configurations in the DPSAC [6].

DPSAC equipped with parallel fins significantly improves thermal efficiency, as shown in Figures 1.3 and 1.4, resulting in a remarkable 57.8% temperature increase at the lowest MFR of 0.0036 kg/s compared to other installations. The thermal performance differed among different orientations of the fins, with parallel fins exhibiting the highest temperatures, thus suggesting their superior efficiency in heat transfer. There is an inverse correlation between the rate at which mass flows and the temperature, meaning that lower flow rates result in higher temperatures. Vertical and opposite fins have been demonstrated to significantly affect air flow by generating large recirculation zones and regions of reduced pressure. This, in turn, modifies the aerodynamic properties and pressure dynamics within the DPSAC. Although these arrangements resulted in increased pressure drops, they did not lead to correspondingly greater temperatures, indicating a compromise in design efficiency. Parallel fins have consistently shown the most effectiveness in rising temperatures, even at lower flow rates, highlighting their better ability to optimize thermal performance in SACs .

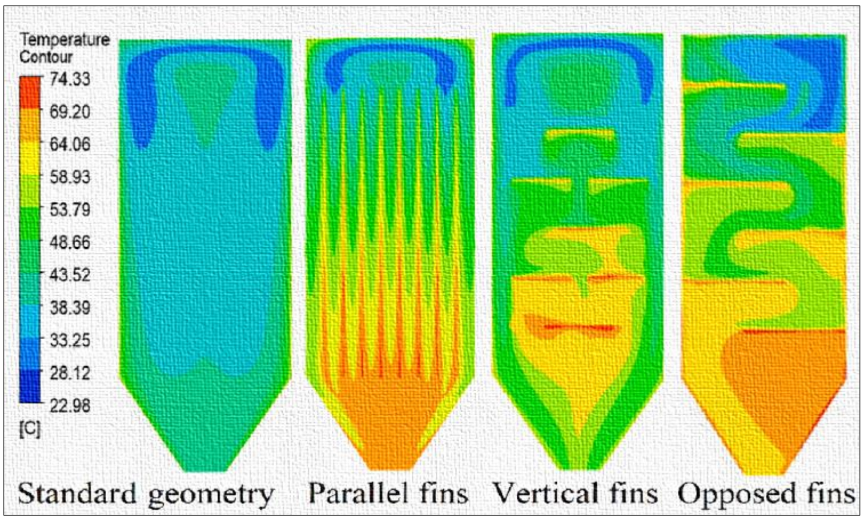

Fig.1.3. MFR of 0.0036 kg/s [6].

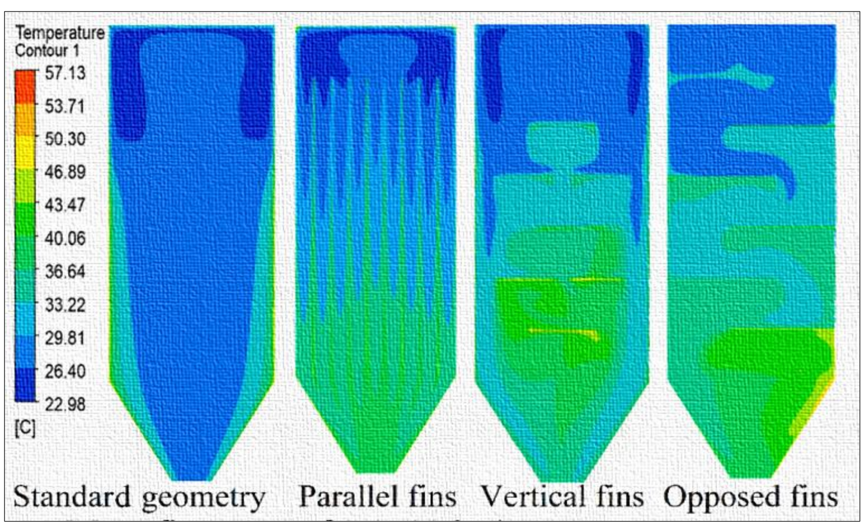

Fig.1.4. MFR of 0.0183 kg/s [6].

In addressing the challenges associated with the low efficiency of solar thermal systems, Salhi et al [7] explore the feasibility of enhancing a DPSAC for solar drying applications. The primary limitation of such systems' inefficient thermal conversion prompted an optimization of the V-shape absorber by modifying its corrugation angle. This study employs CFD techniques, substantiated by experimental data, to simulate the performance of the modified system; this research utilized meteorological data from Mohamed First University in Morocco, characterized by natural and fluctuating weather conditions, to inform the simulations. The methodology hinges on adjusting the corrugation angle from 40 to 180 degrees, as shown in Figure 1.5, where the absorber assumes a flat configuration (used as the reference case).

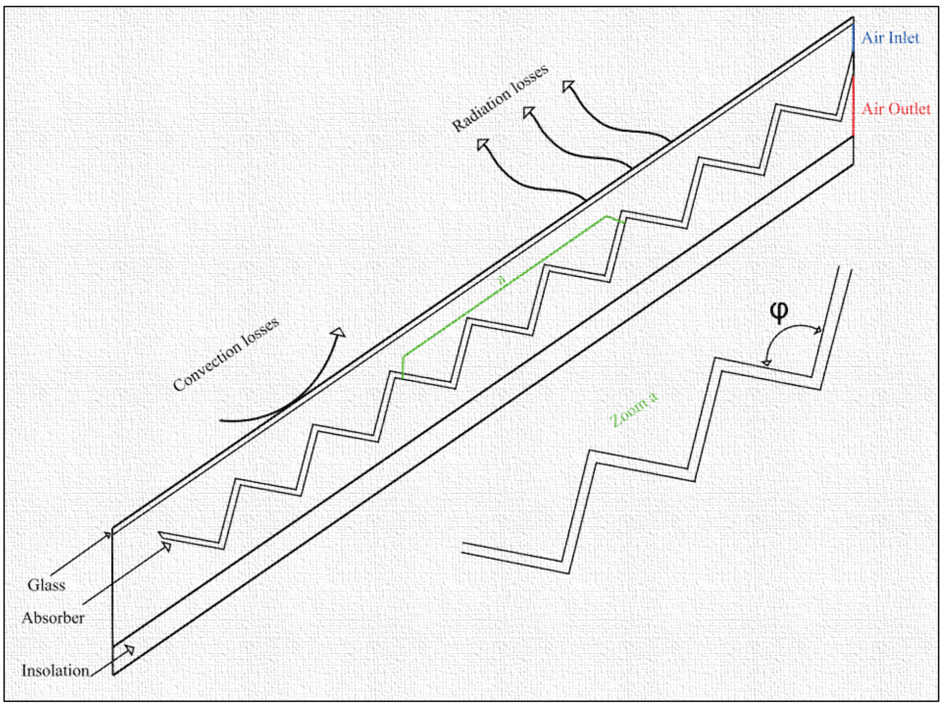

Fig.1.5. Overview of the DPSAC [7].

The dynamics within the collector air gap of the solar thermal system are notably influenced by the angle of the absorber's corrugation; it was observed that secondary recirculation zones become more pronounced at smaller corrugation angles, particularly for angles of 120°, 100° and 80°, the secondary airflow significantly enhances heat extraction from the absorber, marking these regions as hot zones within the solar collector, the results also reveal that the average temperature of the collector air domain and the outlet temperature escalates as the corrugation angle increases, peaking at 100° with temperatures reaching 345.53 K and 365.5

K as shown in Figure 1.6, respectively, before declining. Regarding thermal efficiency, there is a noticeable improvement correlating with the increase in corrugation angle, achieving a maximum efficiency of 86% at a corrugation angle of 100°. Additionally, considering mass flow rates (MFRs), it was found that beyond an MFR of 0.01 kg/s, the average temperature at the collector outlet begins to decrease with higher inlet MFRs, indicating an inverse relationship between mass flow rate and thermal performance at higher flow rates .

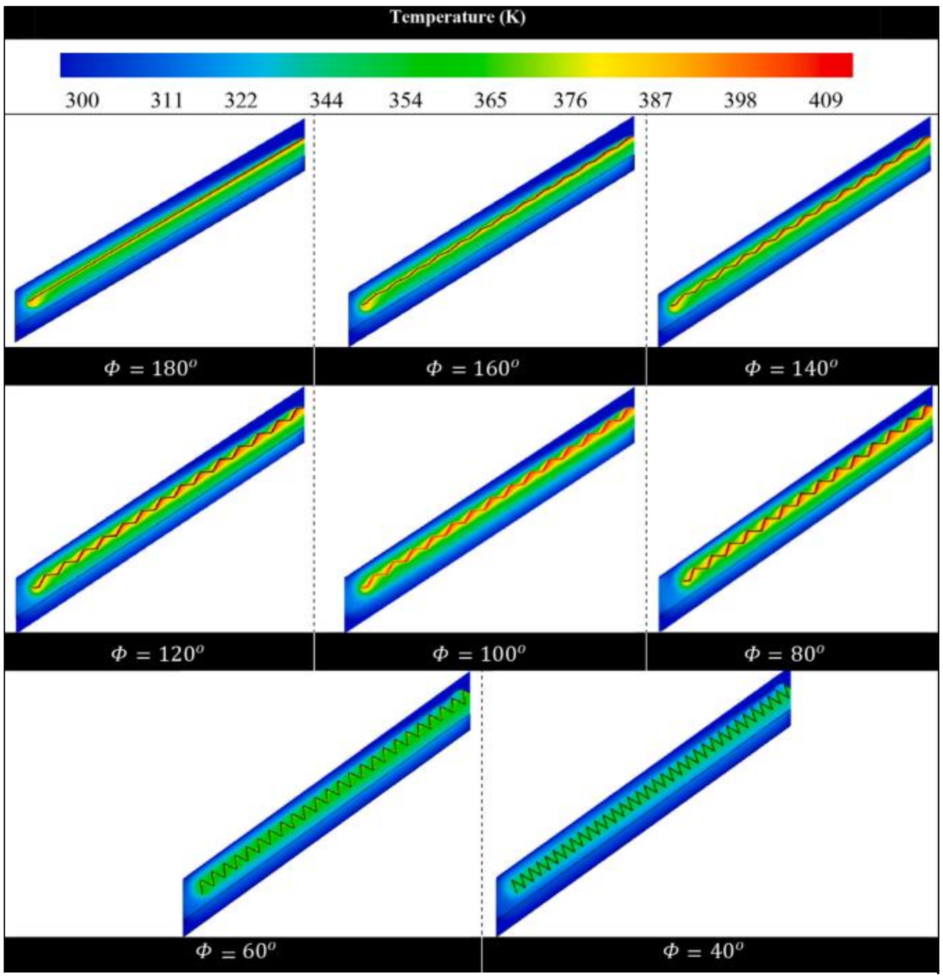

Fig.1.6. Air temperature distribution inside the solar collector for different angles of the corrugated absorber at 1 p.m [7].

1.2. Effect of the Absorber Alate Position on DPSAC

Kumar et al [1]. explored various DPSAC designs and evaluated their performance characteristics through a validated numerical model. The research primarily focuses on optimizing the curved absorber plate position within the system, as shown in Figure 1.7, demonstrating a notable 5°C increase in outlet air temperature when the plate is centrally located between the insulating wall and the transparent glass cover. Additionally, the study reveals that symmetric semi-circular roughened surfaces yield superior performance to symmetric circular shapes due to a higher frequency of vortices reattaching to the absorber plate. The results provide critical insights that enhance the efficiency and effectiveness of solar air heating systems, marking a significant advancement in renewable energy technologies.

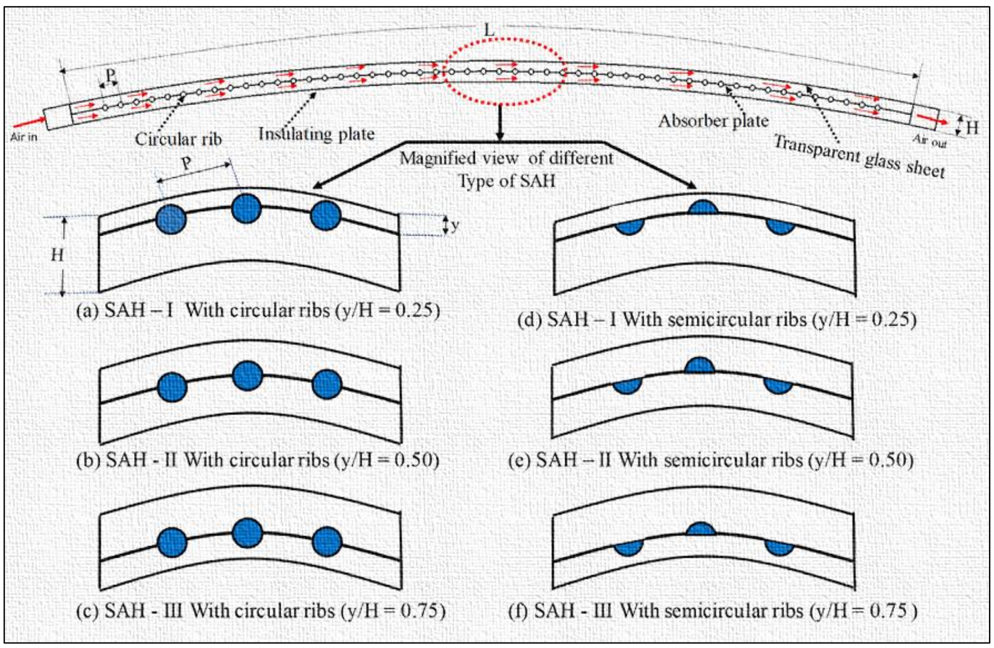

Fig.1.7. Schematic diagram of curved DPSAC with variable relative location of the absorber plates (y/H) [1].

As shown in Figure 1.8, positioning the absorber plate near the top glass results in distinctive thermal behaviors. Specifically, thermal diffusion is predominantly confined below the absorber plate, contrasting with the conditions in the (SAH-I) configuration. Although similar thermal effects are evident in both (SAH-I) and (SAH-III), heat transfer efficiency in (SAH-II) is notably superior. This enhanced performance in (SAH-II) can be attributed to the buoyancy-driven ascent of heated fluid from the absorber plate, which facilitates mixing heated air with colder fluid. Conversely, in the (SAH-I) setup, there is a pronounced tendency for the heated fluid to lose heat to the environment, exacerbated by its closer proximity to the glass. Consequently, (SAH-II) achieves the highest outlet air temperature, followed sequentially by (SAH-III) and (SAH-I) .

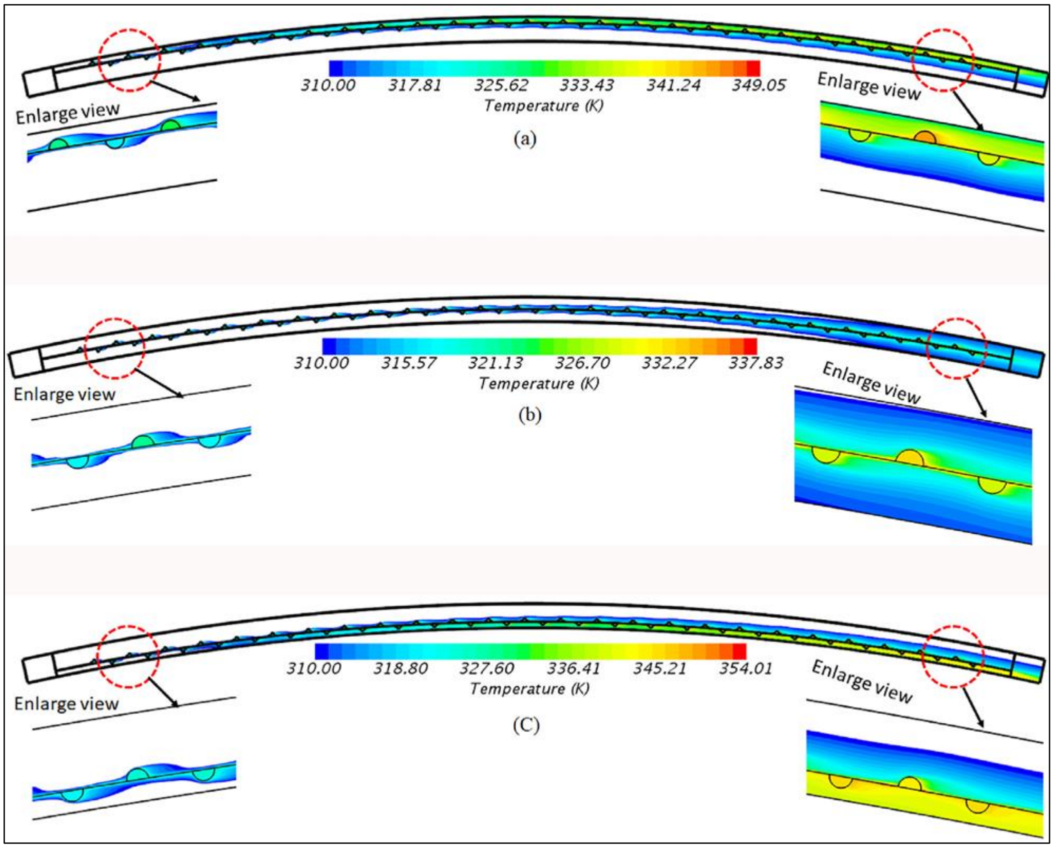

Fig.1.8. Temperature contours at different relative locations of absorber plate (a)-SAH-I, (b)-(SAH-II), and (c)- (SAH-III) [1].

Korti [8]. examined the thermal performance of a DPSAC system, as shown in Figure 1.9, with a particular emphasis on the influence of porous media embedded in the lower channel on system efficiency and temperature distribution. Utilizing numerical simulations CFD, the study systematically investigates the effects of various parameters, including porosity, MFR, solar intensity, and spacing of the absorber-glass, on the dynamic and thermal responses of the solar collector. The objective is to elucidate the role of porous media in enhancing the thermal efficiency of the DPSAC, thereby offering valuable insights for optimizing solar thermal technologies .

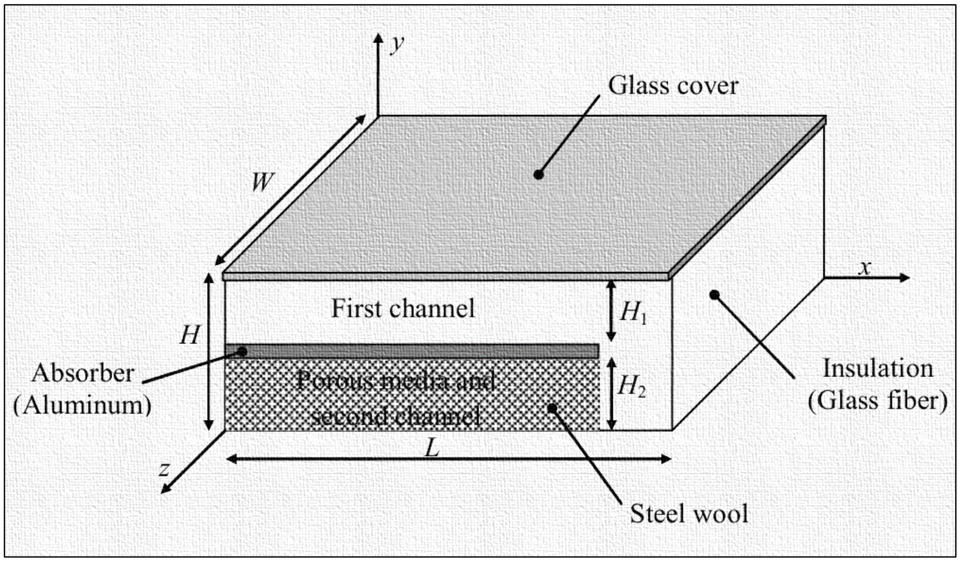

Fig.1.9. Schematic of the DPSAC design [8].

Figure 1.10 illustrates the effect of varying the spacing between the glass-absorber and insulation on the centerline (z = 0.6 m) temperature contours and velocity vector evolution in a SC both with and without porous media. At a constant MFR, altering the channel height (thereby changing the channel section) affects the flow velocity. The data indicate that flow velocity significantly impacts the thermal behavior of the collector. Reducing the glass-absorber spacing increases the mean air velocity in the first channel, decreasing air temperature. Conversely, increasing the absorber-insulation spacing reduces the mean air velocity in the second channel, increasing air temperature. To minimize thermal losses from the top and enhance heat exchange at the bottom, reducing the upper spacing while increasing the lower spacing is practical. As the spacing between the absorber and insulating plate increases, the recirculation zone at the inlet of the second channel becomes broader and taller, enhancing the conduction heat transfer characterized by the recirculation phenomenon. This results in a higher heat transfer from the absorber to the air, increasing the temperature of the circulating air. However, without porous media, the increase in outlet air temperature with greater absorber-insulating plate spacing is significantly higher than with porous media. This indicates that porous media sufficiently enhances conduction heat transfer with reduced spacing, making further increases in absorber-insulating plate spacing less practical when porous media is present .

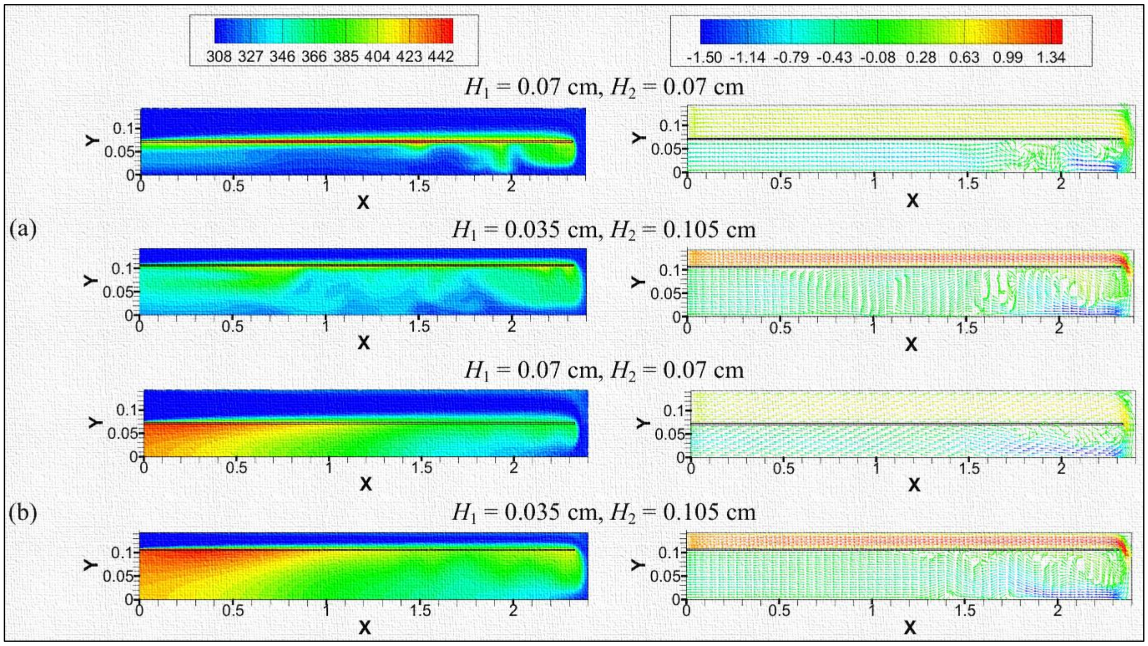

Fig.1.10. Spacing glass-absorber-insulation effect on the centerline (z = 0) temperature and velocity evolution [8].

1.3. Influence of Inlet and Outlet Positions on the Thermal Efficiency in DPSAC

SACs are a practical substitute for traditional fossil fuel technologies in applications such as drying and space heating; They help reduce the impact of climate change. These devices utilize compound parabolic concentrators capable of reaching air temperatures of up to 120°C. To minimize the amount of space needed for installation, it is essential to improve heat transmission efficiency; Chávez-Bermúdez et al [9].studied a parabolic concentrator that has a flat receiver; the study aims to determine the concentrator's ability to recover heat from the interconnected cavity formed by the cover, receiver, and reflectors arranged in a U-shape DPSAC, during operation, air flows through the hollow and enters the duct, producing substantial heat absorption from solar energy, the impact of inlet and outlet positions on the output temperature of the concentrator was investigated using dynamic simulations of four different airflow configurations within the cavity, as shown in Figure 1.11 .

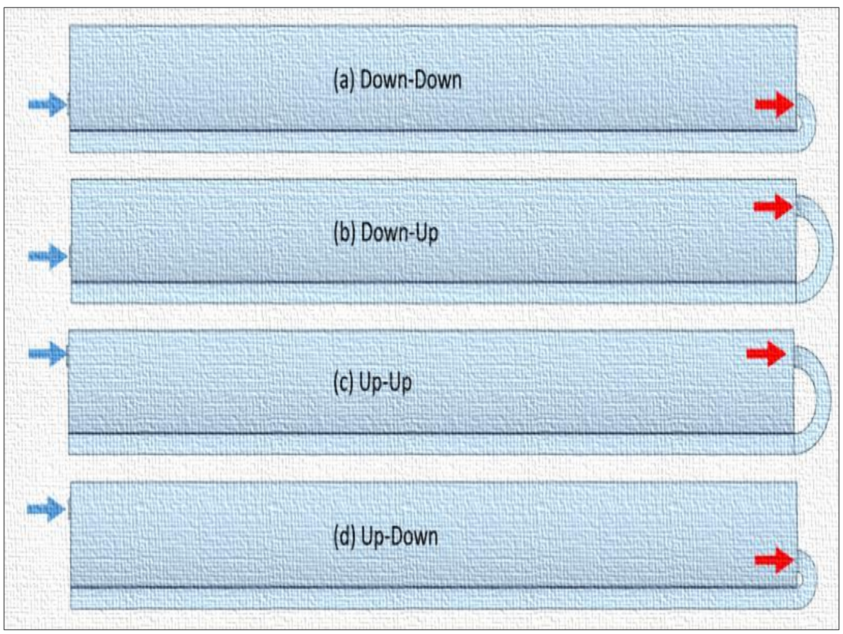

Fig.1.11. Inlet and outlet studied configurations of U-shape DPSAC [9].

In the evaluation of configurations within the compound parabolic concentrator system, the Down–Down configuration demonstrated the highest efficiency at a mass flow rate of 0.01 kg/s, achieving an efficiency of 77.3%; this configuration was notably more effective in optimizing thermal efficiency compared to other setups, highlighting its superior heat transfer capabilities within the double U-pass CPC system, as shown in Figure 1.12 .

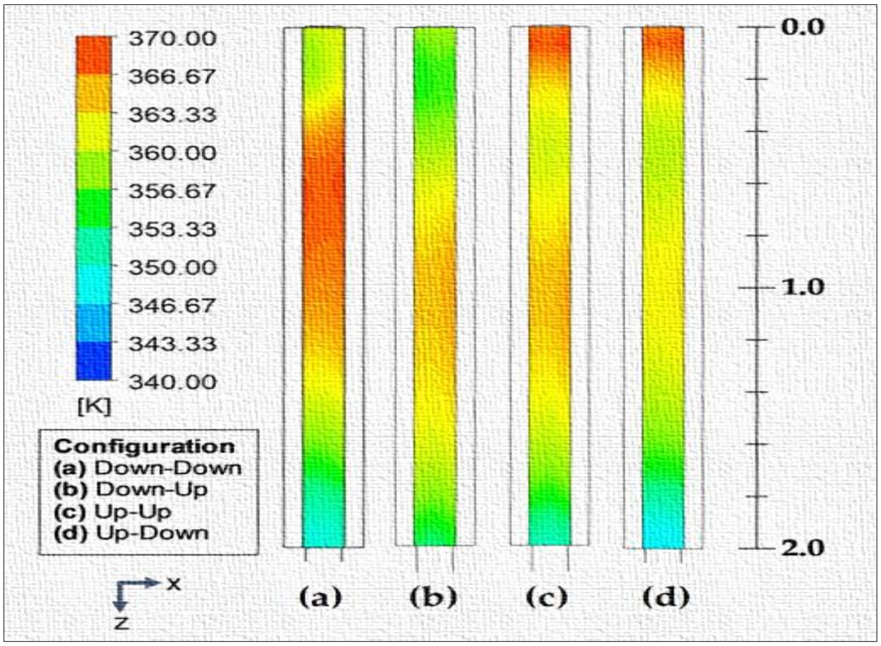

Fig.1.12. Temperature contours of the flat plate receiver [9].

Al-Damook et al [10]. evaluated the influence of different flow arrangements on the thermal efficiency of a solar heater system, the system uses recycled aluminum cans as turbulators for DPSAC. Three designs were examined: co-current (Model A), counter-current (Model B), and U-shape (Model C), as shown in Figure 1.13 .

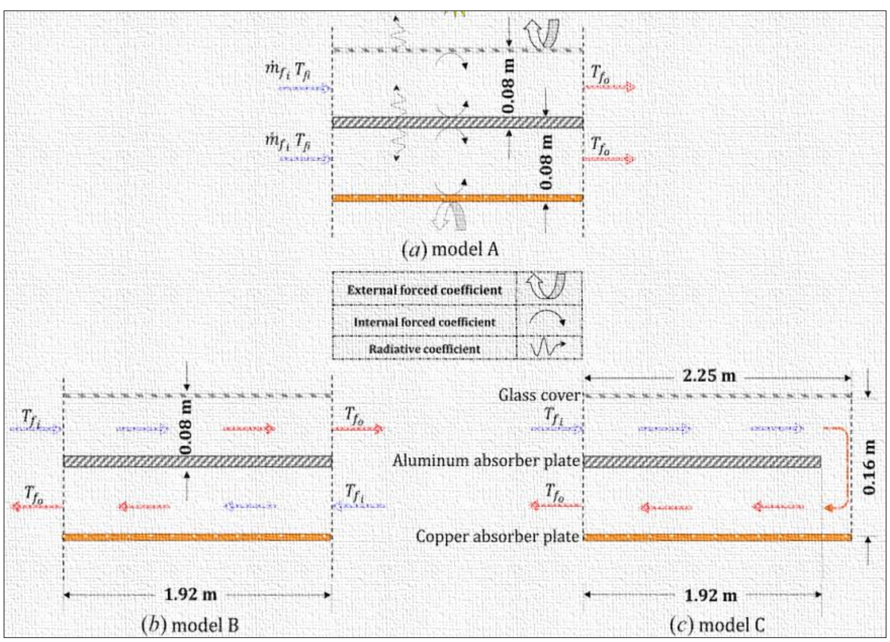

Fig.1.13. Schematics of the three SACs [10].

The U-flow model has the highest thermal effective efficiency (up to 57.42%) compared to the co-current (up to 52.1%) and counter-current (up to 51.6%) efficiencies across the whole range of Reynolds number ($10^3 \leq Re_D \leq 2*10^3$) As shown in Figure 1.14, this is due to the longer length of the air path compared to other models, resulting in the accumulation of heat along the flow channel and causing an increase in the outlet air temperature. It is important to note that enhancing the thermal efficiency of a specific model comes at the cost of reducing the effectiveness of the power fan; for example, the U-flow model necessitates fan power that is approximately 15.7 times greater than the power consumed by the other two types, the power usage of models A and B is 0.364 W each, but model C consumes 6.097 W, among the three models (A, B, and C), the U-flow model (C) has the maximum efficiency.

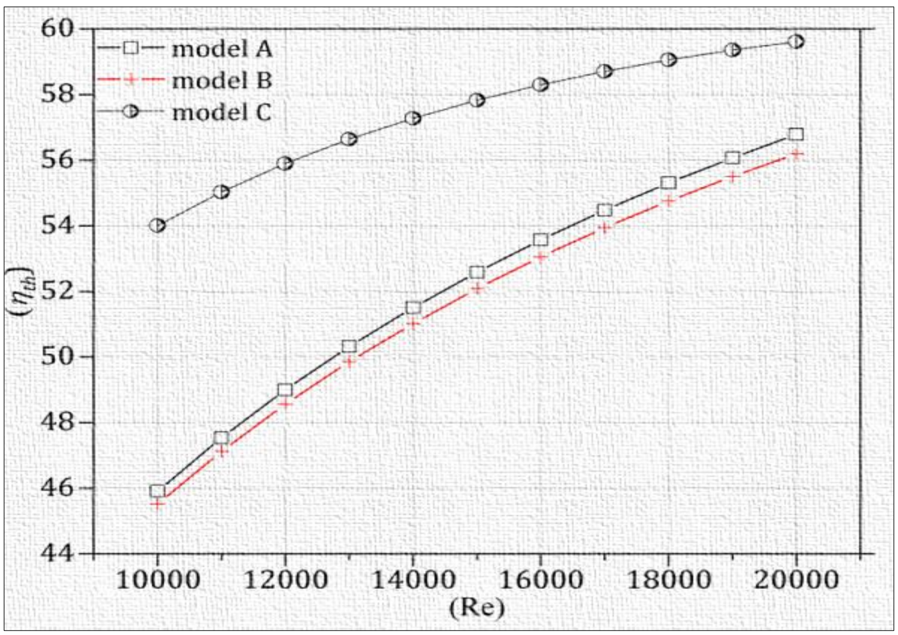

Fig.1.14. The thermal efficiency versus Reynolds number under turbulent condition regime for three models [10].

1.4. Effect of Glazing Gap on a DPSAC

Omojaro et all [12]. explored the thermal efficiency of single and double-pass solar air collectors equipped with a steel wire mesh absorber plate. To evaluate the influence of air MFR on thermal efficiency and output temperature, the rates were adjusted within the range of 0.012 kg/s to 0.038 kg/s. In addition, Figure 1.15 displays a comprehensive design of the SPSAC and DPSAC; the frames used by the collectors were constructed from plywood that was 2 cm in thickness; this design choice was taken to optimize the absorption of solar radiation. Additionally, both the interior and exterior of the frames were painted black. The insulation of each collector consisted of a 2 cm thick layer of Styrofoam, covering all sides and the base to minimize heat loss; the solar air heater frame had a length of 150 cm and a width of 100 cm, and the glazing was made using standard window glass measuring 0.3 cm in thickness. The first and second glass layers were separated by a distance of 3 cm (h), while the second glass layer was separated from the collector base by a distance of 7 cm, to establish a SPASC configuration, the upper-most glass panel of the SAC was detached.

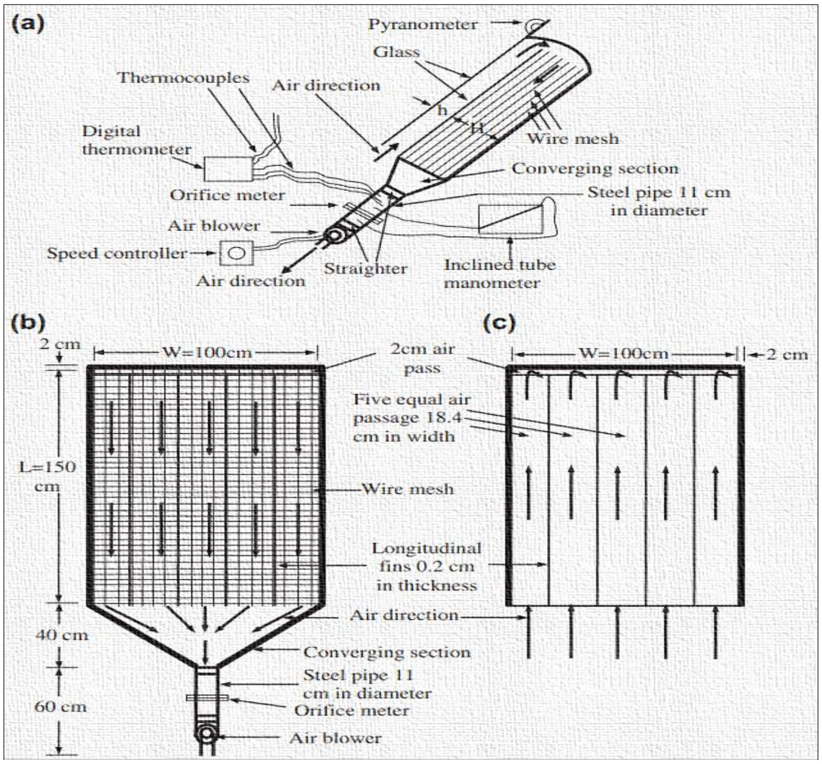

Fig.1.15. SPSAC and DPSAC showing (a) Schematic diagram of the experimental setup, (b) lower pass channel, and (c) upper pass channel [11].

The experiment examined the thermal efficiency of solar air heater systems, explicitly comparing the performance of single and double-pass versions; the SPSAC attained a remarkable maximum thermal efficiency of 59.62%. On the other hand, the DPSAC showed a superior efficiency of 63.74%; the efficiencies were calculated at an air MFR of 0.038 kg/s, demonstrating the higher capability of the double pass system under the same operational conditions. An important observation was that raising the height of the initial pass in the double pass system decreased its thermal efficiency. These findings indicate that the design and structural characteristics significantly affect the system's performance. In addition, it was observed that as the pace at which air MFRs increased, the difference in temperature between the exhaust flow and the surrounding environment decreased, and the drop in temperature differential suggests a decline in the system's ability to retain heat at more excellent MFRs. In addition, incorporating steel wire mesh into these solar air heating systems significantly improved thermal efficiency. This enhancement was especially remarkable when contrasted with conventional SACs, as demonstrated in Figure 1.16 .

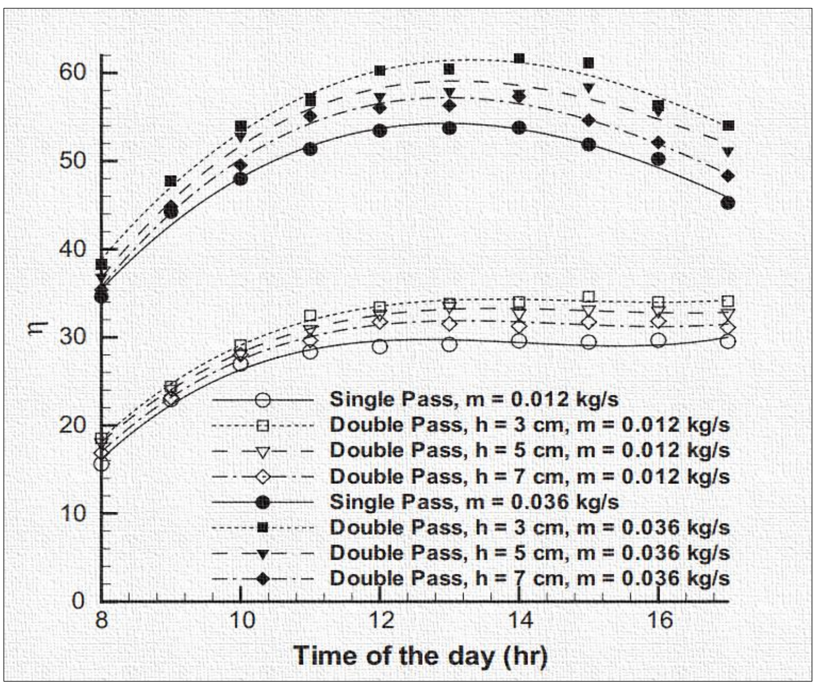

Fig.1.16. Effect of first pass height on the thermal efficiency of a DPSAC compared with SPSAC [11].

1.5. Comparative Effects of Natural and Forced Convection in DPSAC

The thermal performance of two trapezoidal DPSAH was studied by Salih et al [12]. each equipped with double glass covers but differing in their use of a packed bed, was examined. (DPSAH-1) includes a porous medium above the absorber surface, in contrast to (DPSAH-2) as shown in Figure 1.17; both models underwent testing in winter circumstances to assess their performance, with evaluations conducted under natural and forced air circulation .

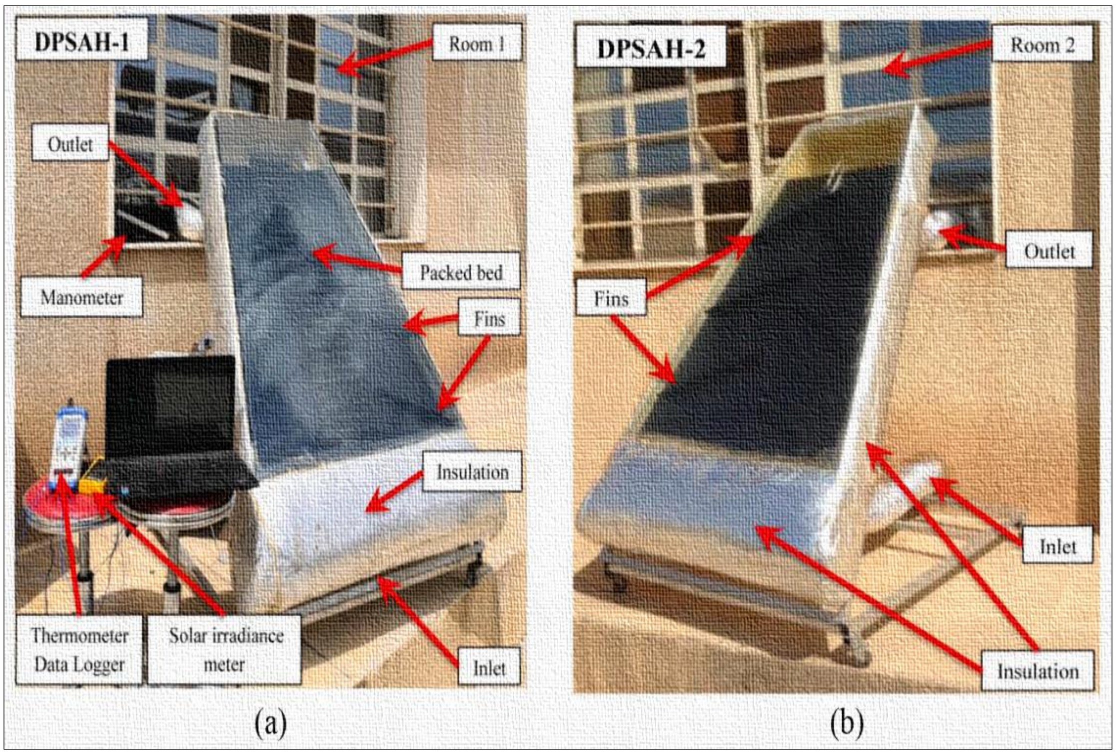

Fig.1.17. Photograph of (a) DPSAH-1 and (b) DPSAH-2 models [12].

The results demonstrate improved efficiency when natural convection conditions are present in both systems. (DPSAH-1) and (DPSAH-2) attained maximum efficiencies of 87% and 82%, respectively, by natural convection, as opposed to 81% and 67% under forced convection with lower air MFRs; an appreciable temperature difference was detected between the natural and forced convection processes: the enhanced efficiency of (DPSAH-1), which integrates a porous medium, highlights the porous medium's significant effect and the air circulation mechanism on the heat transfer rate. Therefore, it can be concluded that (DPSAH-1) performs better than (DPSAH-2), especially in situations when forced convection is needed and greater temperatures are necessary, as shown in Figure 1.18 .

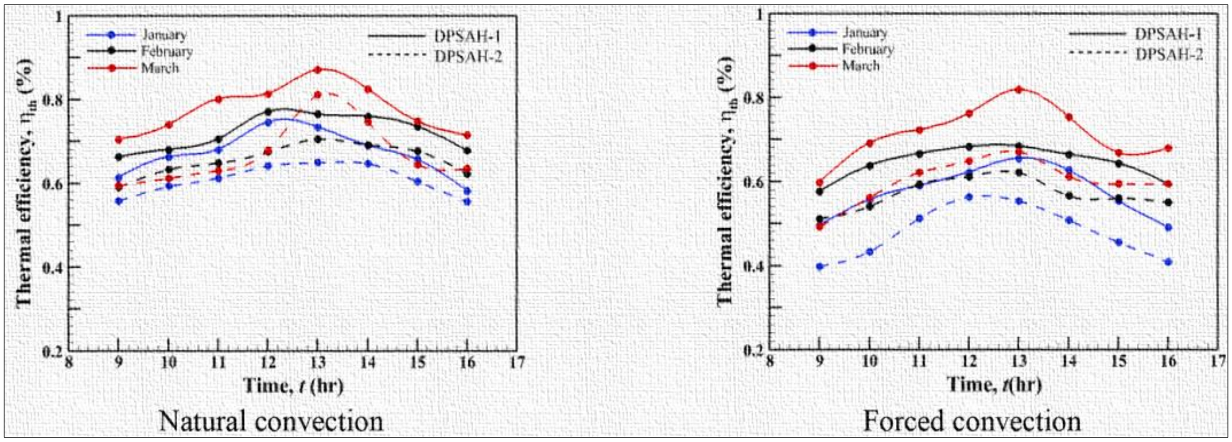

Fig.1.18. ηth between DPSAH-1 and DPSAH-2 [12].

This comprehensive review synthesizes research on the thermal performance and design efficiencies of DPSACs, focusing on the interaction between fin configurations, airflow dynamics, and glazing gaps; the document elaborates on the effects of varying fin configurations, such as parallel, vertical, and opposite arrangements, on the thermal dynamics of DPSACs.

It further investigates the influence of inlet and outlet positions on the thermal efficiency of these systems, assessing the impact under both natural and forced convection conditions. The analysis examines glazing gaps within DPSACs, particularly how air MFRs influence thermal efficiency; the review also contrasts the thermal performance under natural versus forced convection, highlighting the differential effects on system efficiency; key findings include the enhanced performance of systems with parallel fins and U-shaped configurations, which significantly improve thermal efficiency through optimized airflow and heat exchange. Supporting this analysis, the review incorporates detailed schematics and experimental data across various configurations, providing visual and quantitative insights; these include comparative visualizations of fin configurations, temperature contours within the collectors, and efficiency metrics under different airflow conditions. This scholarly review is an essential resource for understanding and advancing the design and operational efficacy of SACs systems.

To conclude, while existing research often emphasizes complex designs to enhance efficiency, our work highlights the effectiveness of simplicity in achieving these improvements.

In the next chapter, we will further explore how our study demonstrates that maintaining simplicity can also lead to substantial increases in the efficiency of SAC systems.

Chapter 2: Experimental Procedures

Experimental Procedures

2.1. Problem Statement

This research aims to evaluate four distinct configurations of DPSAC with absorber-to-glass distances set at 3 cm, 6 cm, 9 cm, and 12 cm, as shown in Figures 2.1-2.2, to determine which configuration achieves the highest efficiency: the objective is to identify the configuration that provides the optimal efficiency. The study will employ experimental methods to measure and compare the outcomes of each configuration under controlled conditions**.**

Fig.2.1. Photo of the four configurations of absorber positions in the DPSAC.

Fig.2.2. Schematic of the experimental setup.

To complement the experimental data and gain deeper insights into the thermal dynamics not readily observable in physical experiments, CFD simulations will be conducted. These simulations will help validate the experimental findings and provide a detailed analysis of the heat transfer and airflow patterns within the DPSAC; by integrating experimental and computational approaches, this research seeks to pinpoint the optimal absorber-to-glass gap and understand the underlying mechanisms affecting DPSAC efficiency.

2.2. Experimental Setup and Materials

This section details the experimental setup and the specific components used in the double-pass solar Air Collectors DPSAC for this study.

2.2.1. Components of the DPSAC

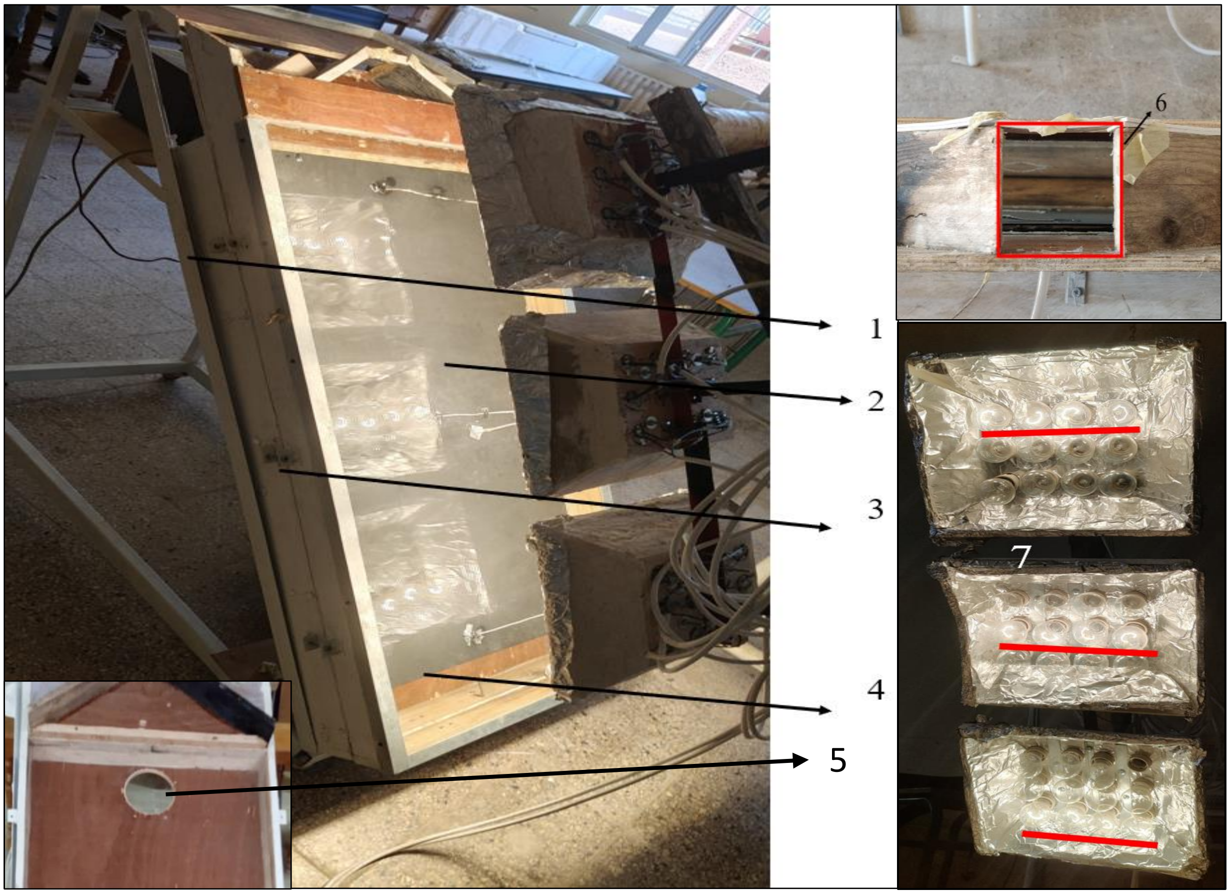

Fig.2 3. Schematic of DPASC parts.

Table.2.1. Key components of the DPASC.

1- Support Stand	4- Absorber plate	7- solar simulator
2- glass cover	5- Inlet	
3- Housing	6- Outlet	

Table 2.2. The DPSAC characteristics.

parameter	symbol	Dimensions
Collector tilt angle	θ	45°
Collector disposition		Parallel to the radiation source
Collector length	L	1.335 m
Collector width	W	63.6 cm
Collector width		
Overall depth flow	-	15.64 cm
U-turn length	-	10.35 cm
Absorber length	-	1.1935 m
Absorber width	-	0.598 m
Absorber surface area	A_{abs}	0.7137 m^2
Absorber plate thickness	-	1.8 mm
Distance between plate and glass cover	-	Variant (3,6,9,12) cm
Glass cover length	-	1.297 m
Glass cover width	-	0.598 m
Glass cover area	-	0.7756 m^2
Glass cover thickness	-	6 mm
Inlet area	-	0.01227 m^2
Outlet area	-	0.004 m^2
Absorber plate absorptivity	α_{abs}	0.92
Glass transmissivity	τ_g	0.92
Glass absorptivity	α_g	0.06
Glass emissivity	ε_g	0.92

Table.2.3. Material characteristics of the DPSAC components.

	Density (ρ) (Kg/m^3)	Specific heat (Cp) (J/(KgK))	Thermal conductivity (λ) (W/mK)
Glass cover	1375	840	0.96
aluminum	2719	871	202.4
wood	700	2310	0.1

2.2. Thermocouple Position in DPSAC

In our DPSAC setup, precise temperature measurement is crucial for evaluating thermal performance effectively: to achieve this, thermocouples are strategically positioned throughout the system, as shown in Figure 2.4 :

1- Absorber Thermocouples:

Top: measures the temperature at the top of the absorber.

Middle: positioned at the midpoint of the absorber for central temperature data.

Bottom: captures the temperature at the bottom of the absorber.

2- Glass Thermocouples:

Interior Glass: located on the inside surface of the glass.

Exterior Glass: positioned on the external surface of the glass.

3- Ambient Thermocouple.

4- Inlet and Outlet Thermocouples:

Inlet Temperature: measures the air temperature as it enters the DPSAC.

Outlet Temperature: records the temperature of the air as it exits the collector, indicating heat transfer efficiency from the absorber to the air.

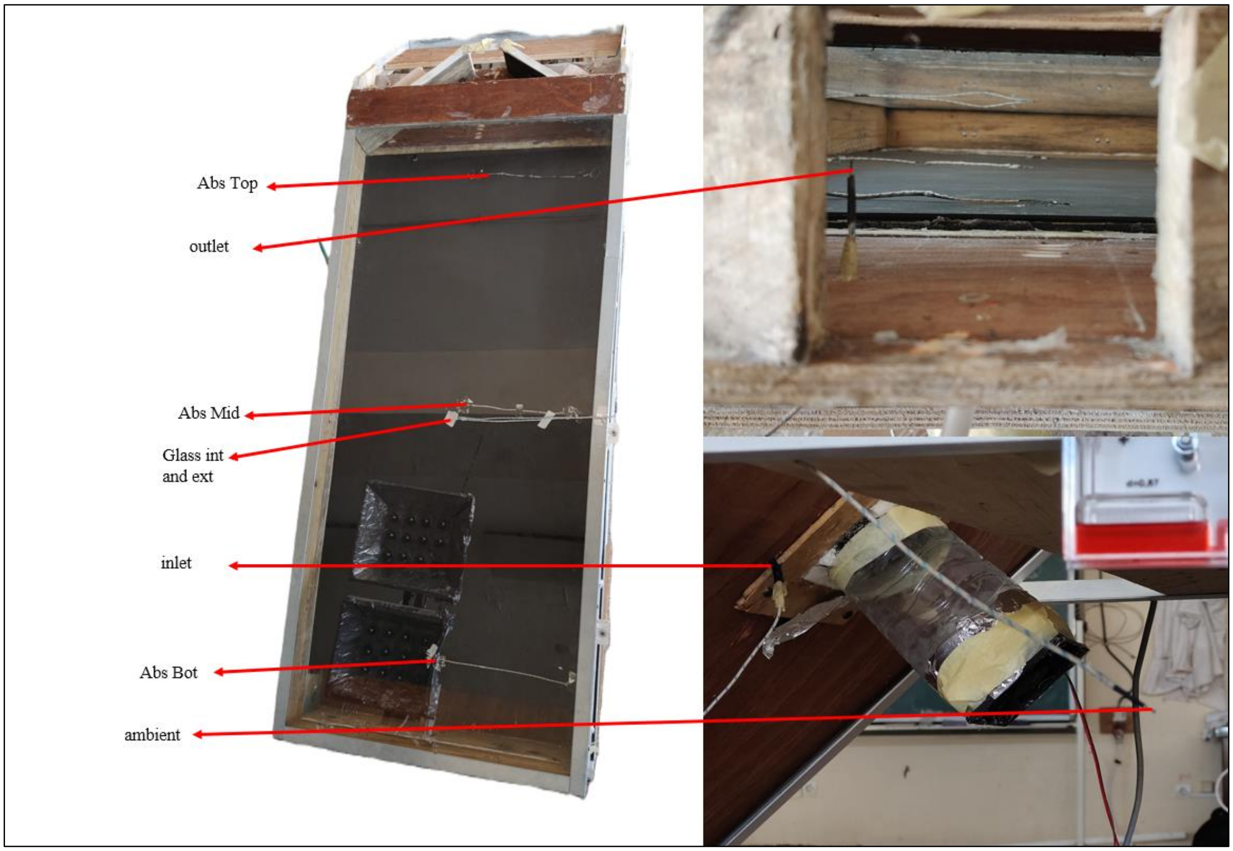

Fig.2.4. Schematic of thermocouple position on the DPSAC.

2.3. Instrumentation and Equipment Overview

Fig.2.6. Solar irradiance meter (SOLAR-100).

Fig.2.5. Data Acquisition System(DAQ9174).

Fig.2.8. Thermo-anemometer (C.A 1266)

Fig.2.7. Thermo-anemometer (6190SI)

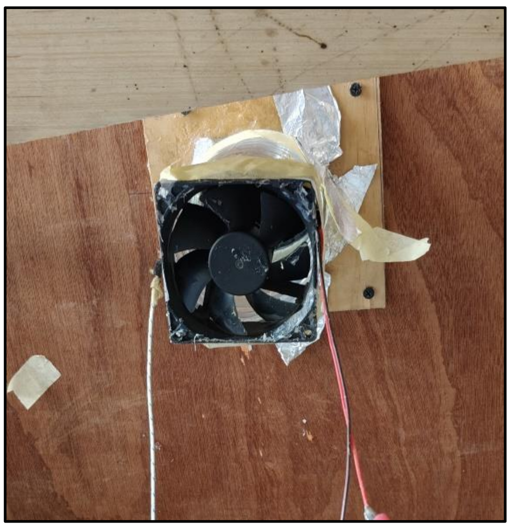

Fig.2.10. Forced-air circulation fan

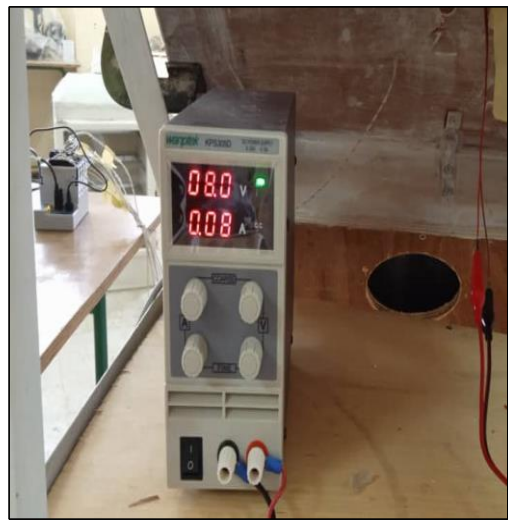

Fig.2.9. Power supply controller

Table.2.4. Devices accuracies.

Devices	Accuracy
solar irradiance meter (SOLAR-100)	±5%
Data Acquisition System(DAQ9174)	50 ppm of sample rate
Thermo-anemometer (C.A 1266)	±3%
Thermo-anemometer (6190SI)	±5%
Power Supply controller (KPS305D)	±0.1%
Thermocouple type (K)	±0.25 °C

2.3. Experimentation Methodology

The experimental setup includes a solar simulator consisting of nine halogen lamps, each rated at 100 watts, which effectively simulate solar radiation, Figure 2.3 illustrates the arrangement and operational details of these lamps; the solar irradiance (I) measured was 270 W/m², as measured by a solar meter, as shown in Figure 2.6,

Airflow through the system is regulated using a booster fan at the inlet, as shown in Figure 2.9, which is controlled by a DC power supply controller, as shown in Figure 2.10. The fan was set to operate at 0.8 volts and 0.08 amperes for four configurations; temperature variations within the collector are meticulously recorded over a 75-minute interval using a data acquisition system (DAQ) connected to a computer, as shown in Figure 2.6. The data is processed and visualized through the LabVIEW software, as shown in Figure 2.11.

To assess the airflow characteristics at the inlet, the velocity is measured using a Thermo-anemometer (model C.A 1266), as shown in Figure 2.7. Additionally, the mass flow rate at the outlet is determined using another Thermo-anemometer (model 6190SI), as shown in Figure 2.8.

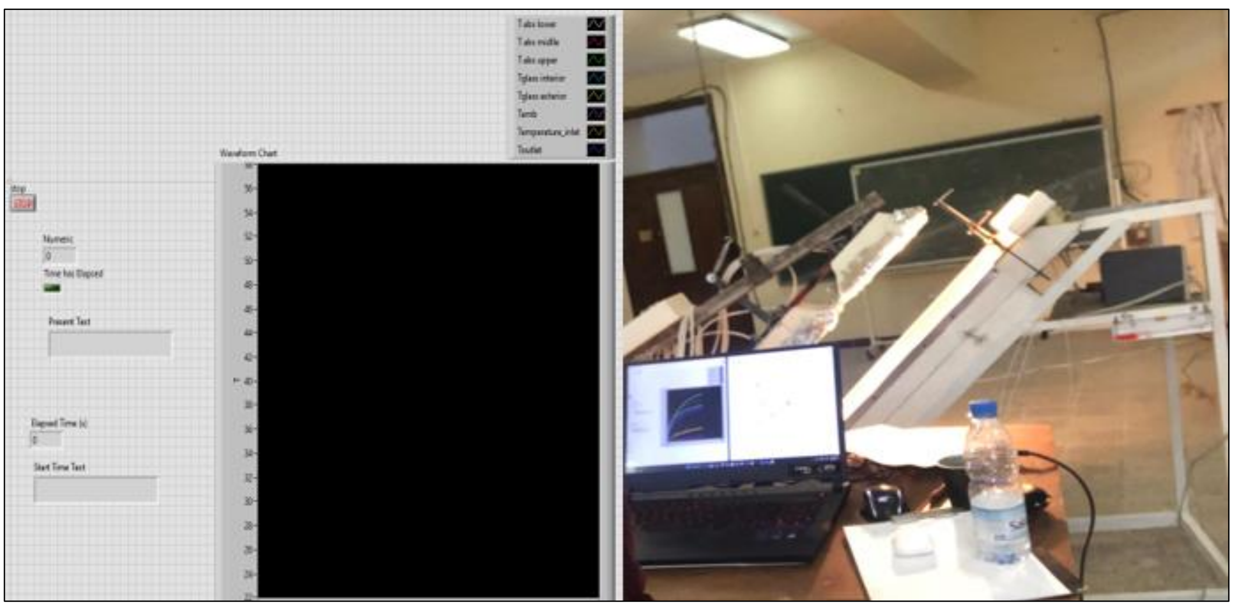

Fig.2.9. LabVIEW

Table.2.5. Measured velocities of four configurations.

Configuration	V inlet
3 cm	0.35 m/s
6 cm	0.41 m/s
9 cm	0.45 m/s
12 cm	0.50 m/s

In conclusion, this chapter has rigorously detailed the experimental methodologies implemented to assess the effects of varying gap distances between the absorber plate and the glass cover within DPSAC. Through systematic investigation of these variations, the study constructs a robust framework for understanding how different configurations impact the thermal dynamics of the system. The methodologies outlined here are designed to be replicable and are founded on stringent scientific principles, aiming to yield reliable and significant data.

To augment the realism and depth of our experimental observations, CFD simulation will be undertaken. These simulations are intended to complement the physical experiments by providing a granular view of the fluid dynamics and thermal interactions that are not readily observable through experimental methodologies alone. The forthcoming chapter will thoroughly discuss the integration of CFD simulations, ensuring a holistic analysis synthesizing theoretical insights with empirical findings. The outcomes from this research's experimental and computational simulation phases will be exhaustively analyzed and discussed in Chapter Four.

Figure 2.3 below illustrates the transition process from experimental procedures to CFD simulation, providing a visual roadmap of the methodological flow of this research.

Fig.2.10. Integrating experimental measurements and CFD Analysis for DPSAC evaluation flowchart.

Chapter 3:CFD Modeling

CFD Modeling

This section will discuss the importance and objectives of using CFD to analyze the DPASC.

; the CFD simulations for this project were conducted using *ANSYS Fluent* within the *ANSYS WORKBENCH 2019 R3* environment. *ANSYS WORKBENCH* facilitated the management of the simulation workflow, including geometry creation, meshing, and project organization. *ANSYS Fluent* was employed for detailed solver settings and fluid flow modeling.

The main objectives of the CFD modeling in this project are:

1- To understand the airflow and temperature distribution within the DPSAC.

2- To evaluate the impact of different absorber positions on the thermal performance of the collector.

3- To validate the CFD model against experimental data to ensure its accuracy and reliability.

4- To conduct a sensitivity analysis of various parameters affecting the system's performance.

By achieving these objectives, the CFD model will contribute to optimizing the DPSAC design, potentially leading to improved efficiency and performance in practical applications.

3.1. Model Assumptions

The fluid is considered air, with constant properties throughout the analysis.

The air is treated as an incompressible fluid.

Three-dimensional (3-D) and transient time analysis.

Turbulent flow.

3.2. Mathematical Formulations

3.2.1. Governing Equations

Continuity Equation (Conservation of Mass) :

$$\frac{\partial u}{\partial x}+\frac{\partial v}{\partial y}+\frac{\partial w}{\partial z}=0 \tag{3.1}$$

Momentum Equation :

X-direction :

$$\rho_f\left(\frac{\partial u}{\partial t}+u\frac{\partial u}{\partial x}+v\frac{\partial u}{\partial y}+w\frac{\partial u}{\partial z}\right)=-\frac{\partial P}{\partial x}+\mu f\left(\frac{\partial^2 u}{\partial x^2}+\frac{\partial^2 u}{\partial y^2}+\frac{\partial^2 u}{\partial z^2}\right) \tag{3.2}$$

Y-direction :

$$\rho_f\left(\frac{\partial v}{\partial t}+u\frac{\partial v}{\partial x}+v\frac{\partial v}{\partial y}+w\frac{\partial v}{\partial z}\right)=-\frac{\partial P}{\partial y}+\mu f\left(\frac{\partial^2 v}{\partial x^2}+\frac{\partial^2 v}{\partial y^2}+\frac{\partial^2 v}{\partial z^2}\right) \tag{3.3}$$

Z-direction :

$$\rho_f\left(\frac{\partial w}{\partial t}+u\frac{\partial w}{\partial x}+v\frac{\partial w}{\partial y}+w\frac{\partial w}{\partial z}\right)=-\frac{\partial P}{\partial z}+\mu f\left(\frac{\partial^2 w}{\partial x^2}+\frac{\partial^2 w}{\partial y^2}+\frac{\partial^2 w}{\partial z^2}\right) \tag{3.4}$$

Equation of energy:

$$(\rho c)_f\left(\frac{\partial T_f}{\partial t}+u\frac{\partial T_f}{\partial x}+v\frac{\partial T_f}{\partial y}+w\frac{\partial T_f}{\partial z}\right)=\lambda_f\left(\frac{\partial^2 T_f}{\partial x^2}+\frac{\partial^2 T_f}{\partial y^2}+\frac{\partial^2 T_f}{\partial z^2}\right) \tag{3.5}$$

3.2.2. Turbulence Modeling

$k-\epsilon$ **Turbulence model** :

$$\frac{\partial(\rho k)}{\partial t}+\frac{\partial(\rho u_j k)}{\partial x_j}=\frac{\partial}{\partial x_j}\left(\left(\mu+\frac{\mu_t}{\sigma_k}\right)\frac{\partial k}{\partial x_j}\right)+P_k+D_k \tag{3.6}$$

$$\frac{\partial(\rho\epsilon)}{\partial t}+\frac{\partial(\rho u_j\epsilon)}{\partial x_j}=\frac{\partial}{\partial x_j}\left(\left(\mu+\frac{\mu_t}{\sigma_\epsilon}\right)\frac{\partial\epsilon}{\partial x_j}\right)+P_\epsilon+D_\epsilon+\rho C_1 S_\epsilon \tag{3.7}$$

Production Modeling :

Turbulent Kinetic Energy k

$$p_{k=}\mu_t S^2 \tag{3.8}$$

Turbulent Dissipation Rate ϵ

$$p_{\epsilon=}C_{\epsilon 1}\frac{\epsilon}{k} \tag{3.9}$$

Dissipation Modeling :

Turbulent Kinetic Energy k

$$D_k=-\rho\epsilon \tag{3.10}$$

Turbulent Dissipation Rate ϵ

$$D_\epsilon=-\rho C_{\epsilon 2}\frac{\epsilon^2}{k+\sqrt{\nu\epsilon}} \tag{3.11}$$

Modeling of Turbulent Viscosity μ_t :

$$\mu_t=C_\mu\frac{k^2}{\epsilon} \tag{3.12}$$

Model Coefficients :

$C_{\epsilon 1}=1.44, C_{\epsilon 2}=1.9, \sigma_k=1, \sigma_\epsilon=1.22$

3.2.3. Radiation Modeling

The Surface-to-Surface (S2S) radiation model was employed to accurately account for the radiative heat transfer between various surfaces within the collector.

Radiosity (j) Equation : $j_i = \varepsilon_i \sigma T_i^4 + (1-\varepsilon_i) G_i$ (3.13)

Irradiation(G) Equation : $G_i = \sum_{j=1}^{n} F_{ij} j_j$ (3.14)

ε_i : emissivity of the surface i.

σ : Stefan-Boltzmann constant $(5.67 \times 10^{-8} W / m^2 K^4)$.

T_i : absolute temperature of surface i.

G_i : the total incident radiative energy on surface i.

F_{ij} : view factor from surface j to surface i.

Net Radiative Heat Flux ($q_{rad,i}$) : $q_{rad,i} = \varepsilon_i \sigma (T_i^4 - G_i)$ (3.15)

3.2.4. Dimensionless Numbers

Nusselt number

$$Nu = \frac{hD_h}{\lambda} \tag{3.16}$$

$$D_h = \frac{4A_c}{P} \tag{3.17}$$

Grashof Number

$$Gr_L = \frac{g\beta\Delta T L_c^3}{v^2} \tag{3.18}$$

Prandtl number

$$\Pr = \frac{\mu Cp}{\lambda} \tag{3.19}$$

Rayleigh number

$$Ra = Gr_L \Pr \tag{3.20}$$

Thermal Efficiency

Thermal efficiency of the (DPSAC) can be expressed as the ratio of absorbed energy by air to the solar irradiance [2].

$$\eta_{th} = \frac{\dot{m}_a cp_a (T_{out} - T_i\ )}{A_{abs} I} \tag{3.21}$$

$\dot{m}_a$: air mass flow rate (kg / s).

cp_a : air specific heat capacity (J / kgK).

T_{out} : outlet temperature (K).

T_i : ambient temperature(K).

A_{abs} : absorber surafce (m^2).

I : solar irradiance (W / m^2).

3.3. Finite Volume Method

The Finite volume method (FVM) begins with the integral form of the conservation equations. The solution domain is divided into a finite number of contiguous control volumes (CVs), and the conservation equations are applied to each (CV), containing a computational node at its centroid, where the variable values are calculated. Interpolation is used to express variable values at the (CV) surfaces regarding the nodal (CV-center) values. Surface and volume integrals are approximated using suitable quadrature formulas. The (FVM) can accommodate any grid, making it suitable for complex geometries. The grid defines the control volume boundaries and does not need to be related to a coordinate system. The method is inherently conservative, ensuring that surface integrals representing convective and diffusive fluxes are identical for the (CVs) sharing the boundary; as shown in Figure 3.1, A cell containing node P now has six neighboring nodes identified as west, east, south, and north, bottom and top (W, E, S, N, B, T). As before, the notation w, e, s, n, b and t is used to refer to the west, east, south, north, bottom and top cell faces respectively [13].

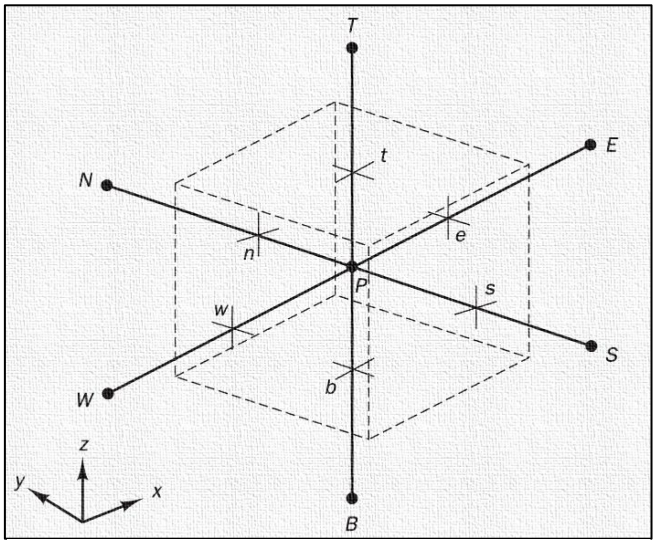

Fig.3.1. 3-D cell [13].

3.4. Simulation Procedure in ANSYS Fluent

The workflow for the CFD simulation follows the standard *ANSYS Fluent* project setup for Fluid Flow (Fluent), as shown in Figure 3.2. This includes steps for geometry creation in *SpaceClaim*, Mesh generation, Setup configuration, solution computation, and results analysis.

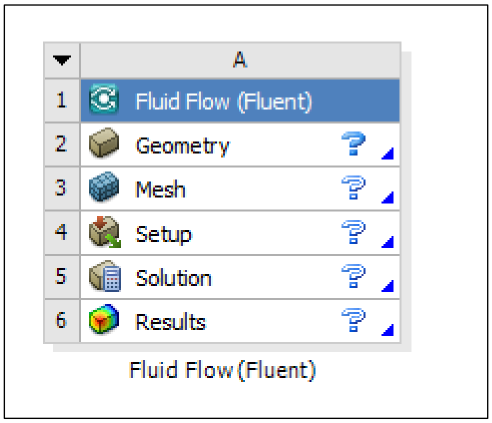

Fig.3.2. Analysis system Fluent.

3.4.1 Geometry Creation

The geometry was created in *SpaceClaim*, a comprehensive 3D modeling environment.

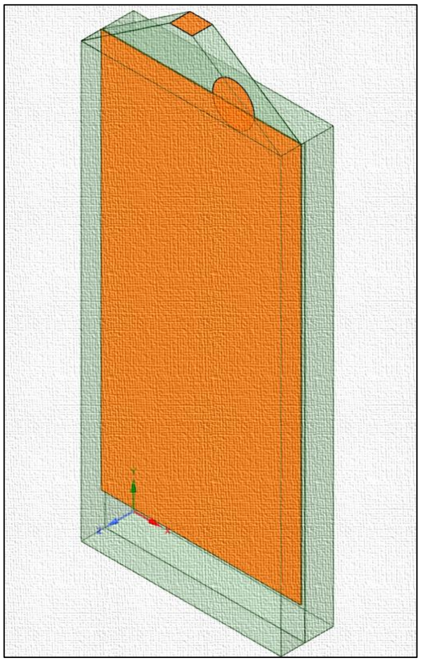

Fig.3.3. 3-D model.

3.4.2. Mesh Generation

The mesh type used is tetrahedral, which is an unstructured mesh. A specific mesh size was applied to capture the geometry accurately; the boundary conditions were defined using named selections in the *ANSYS* meshing tool.

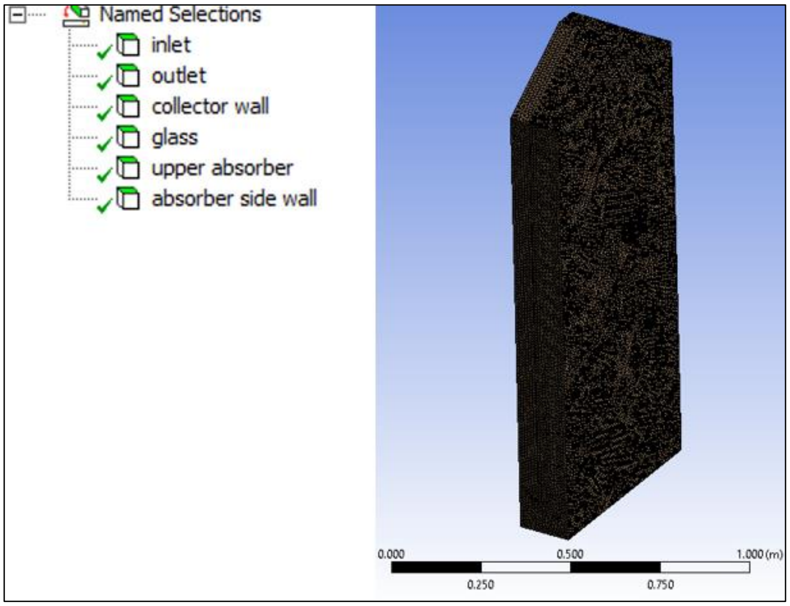

Fig.3.4. Mesh configuration.

3.4.2.1. Mesh Quality

Mesh quality is a critical factor in ensuring the accuracy and stability of CFD simulations. High-quality mesh elements contribute to the precision of the numerical solution and reduce the likelihood of convergence issues. Two important metrics used to assess mesh quality are skewness and orthogonal quality; skewness measures the deviation of an element from an ideal shape. High skewness values indicate poor-quality elements, which can negatively impact the simulation results. Orthogonal quality represents the relationship between an element and its adjacent elements. It assesses how well the elements align with the flow direction and each other, influencing the accuracy of the gradient calculations, as shown in Figure 3.5 [14].

As shown in Figure 3.6, the mesh metrics spectrum visually represents these quality metrics, highlighting areas where the mesh may need improvement. Our results show that the average skewness and orthogonal quality are 0.22354 and 0.77147, respectively.

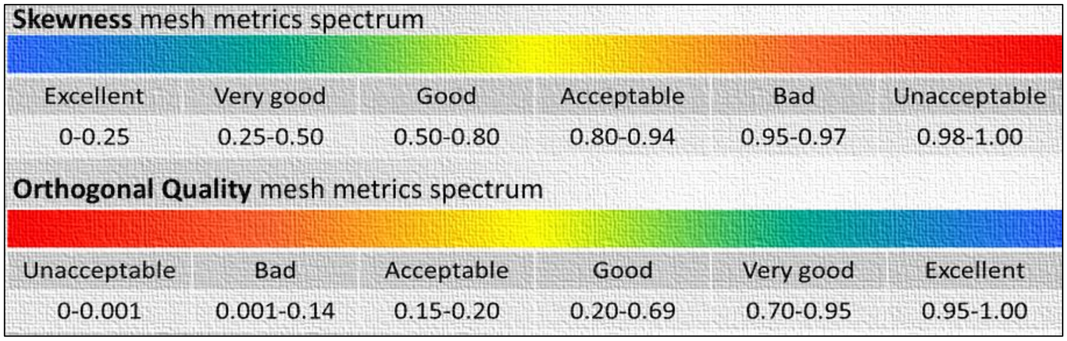

Fig.3.5. Mesh metric spectrum: skewness and orthogonal quality [14].

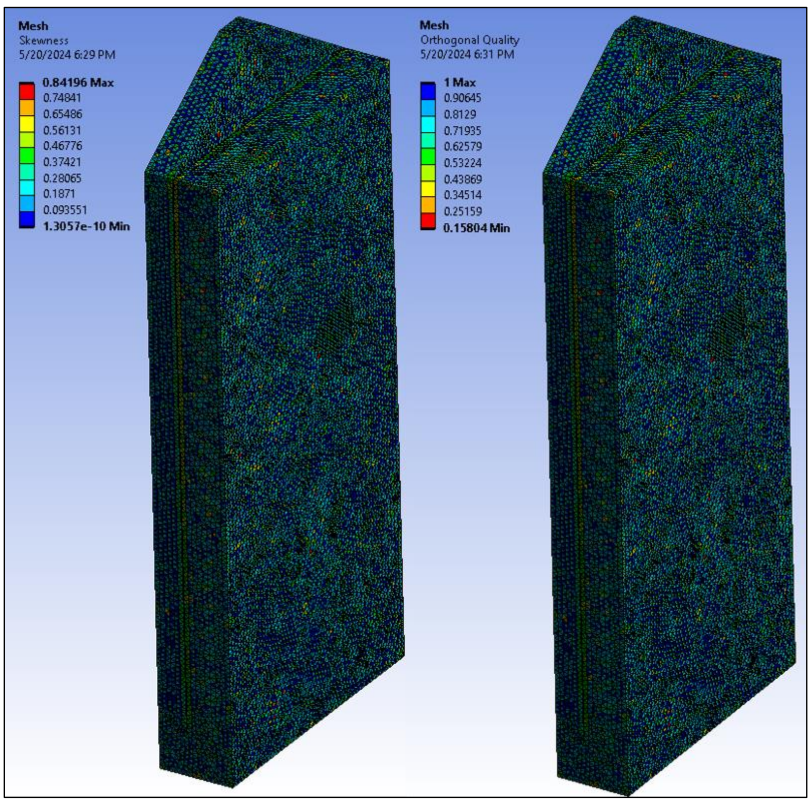

Fig.3.6. Skewness and orthogonality distribution of the mesh.

3.4.2.2. Mesh Independence

Table. 3.1. Mesh configurations tested.

Fig.3.7. Mesh independence tested.

3.4.3. Setup and Solution Methods

The simulation is conducted under transient conditions with gravity activated: the energy equation and the realizable k-epsilon turbulence model with thermal effects are enabled: the Surface to Surface (S2S) radiation model is employed to account for radiative heat transfer.

Table 3 mentions the physical properties of the materials in the previous chapter, except for the fluid (air).

Table.3.2. Physical properties of air.

Density (ρ) (Kg/m^3)	Specific heat (Cp) (J/(KgK))	Thermal conductivity (λ) (W/mK)	viscosity (μ) (Kg/ms)
1.225	1006	0.0242	1.7894E-05

3.4.3.1. Boundary Conditions

inlet $\rightarrow$ velocity inlet $\rightarrow$ varied (0.35,0.41,0.45 and 0.50 m/s)

outlet $\rightarrow$ pressure outlet

collector wall $\rightarrow$ wall

upper absorber $\rightarrow$ wall

glass $\rightarrow$ wall $\rightarrow$ mixed

the hydraulic diameter calculated $D_h = 0.297m$

The residuals were set to (1E-4), and the heat transfer coefficient of the glass was calculated using the external environmental conditions according to the following formulation [15]:

$$Nu = \left(0.825 + \frac{0.387 Ra_L^{1/6}}{[(0.492/\Pr)^{9/16}]^{8/27}} \right)^2 , \qquad h = 3.2655(W/m^2K\ ) \tag{3.22}$$

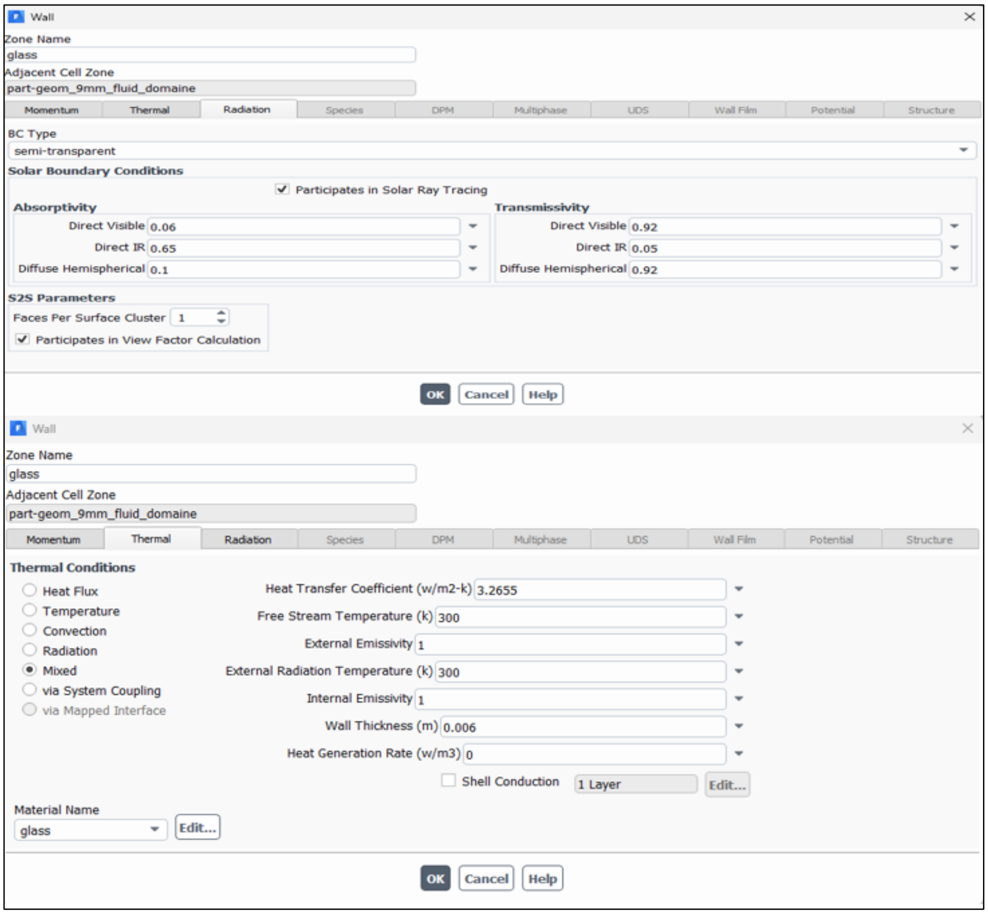

Fig.3.8. Setting the glass boundaries.

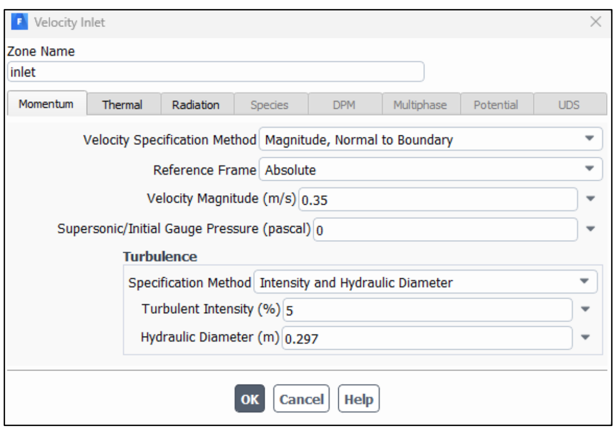

Fig.3.9. Setting the inlet boundaries.

3.4.3.2. Solution Setup

The duration of the experimental procedure was 75 minutes (4500 seconds), in the simulation, a time step size of 10 seconds was utilized, resulting in a total of 450 time steps. Each time step was allowed a maximum of 15 iterations to ensure convergence.

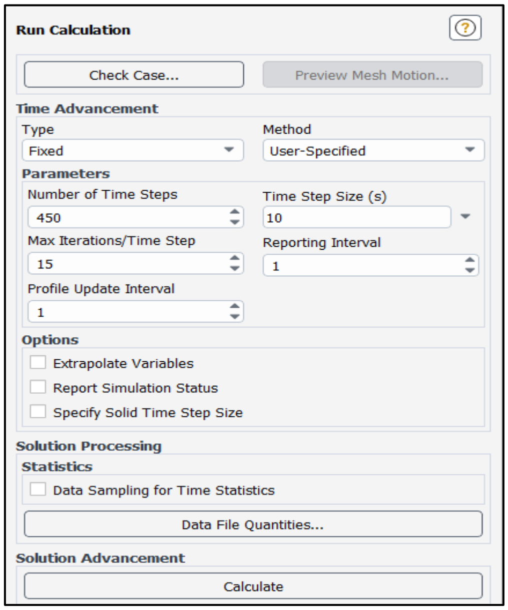

Fig.3.10. Setting the simulation time parameter.

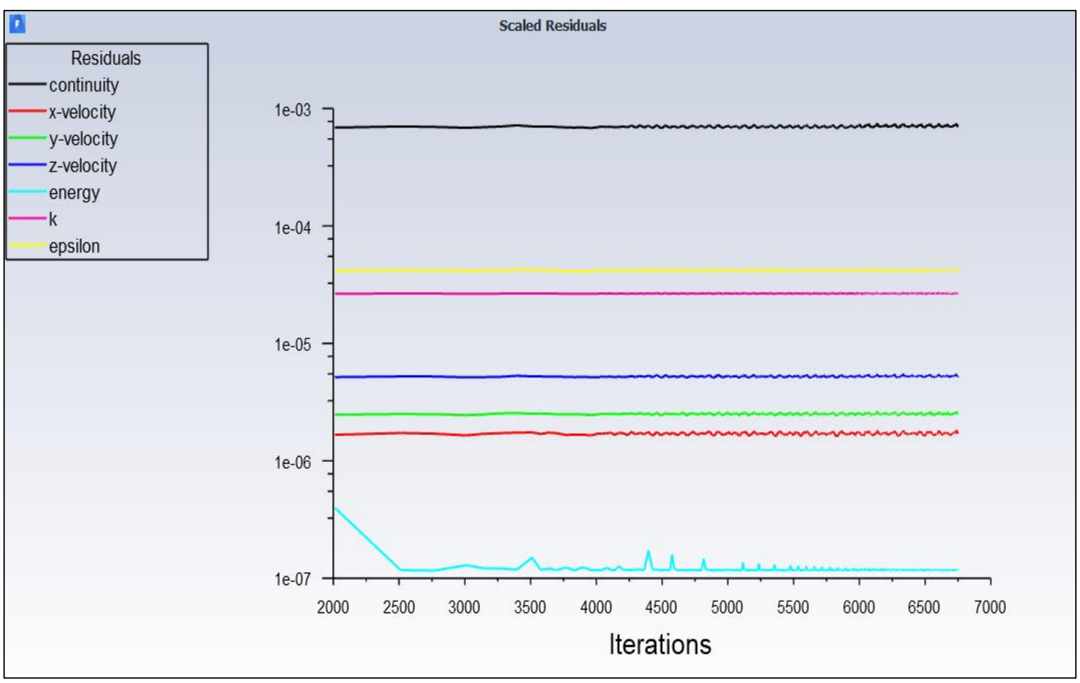

Fig.3.11. Residual convergence plot of 3cm.

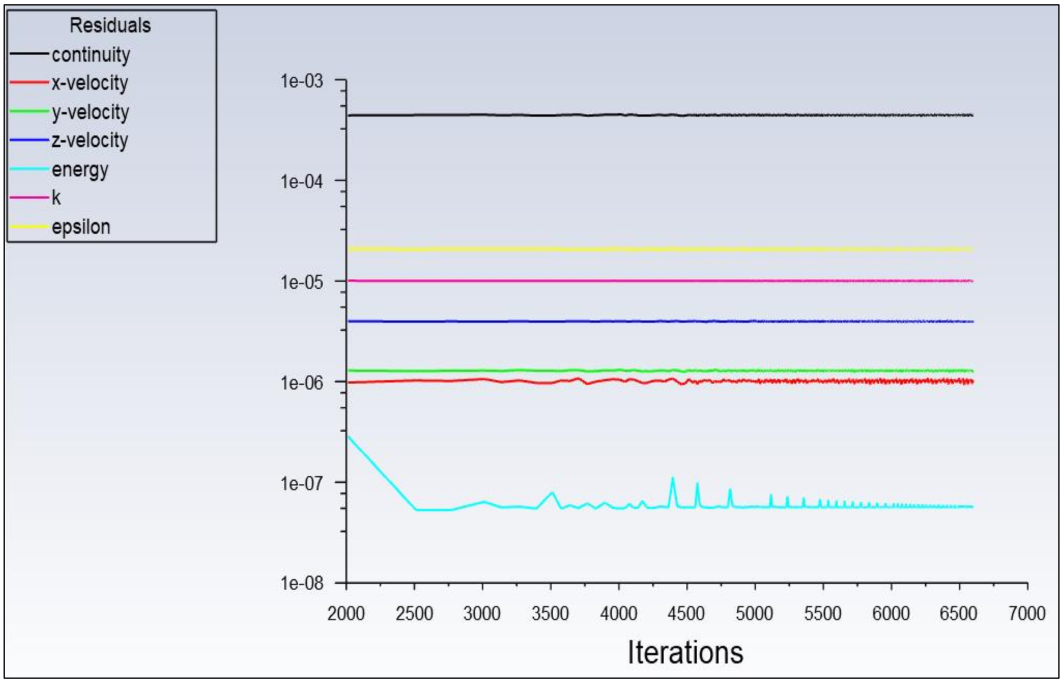

Fig.3.12. Residual convergence plot of 6cm.

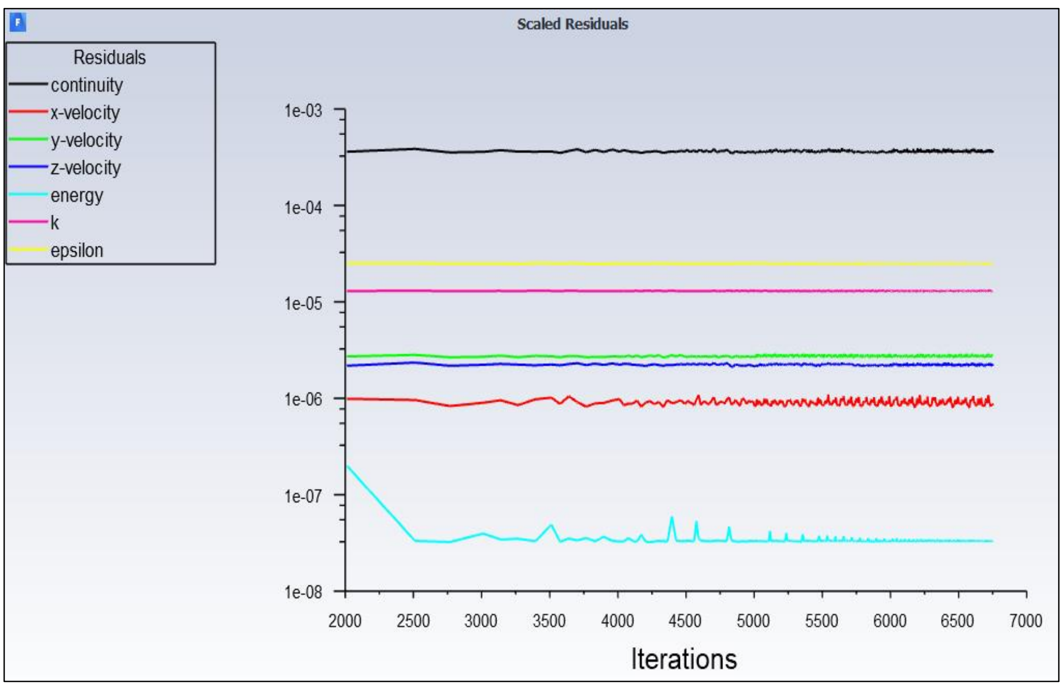

Fig.3.13. Residual convergence plot of 9cm.

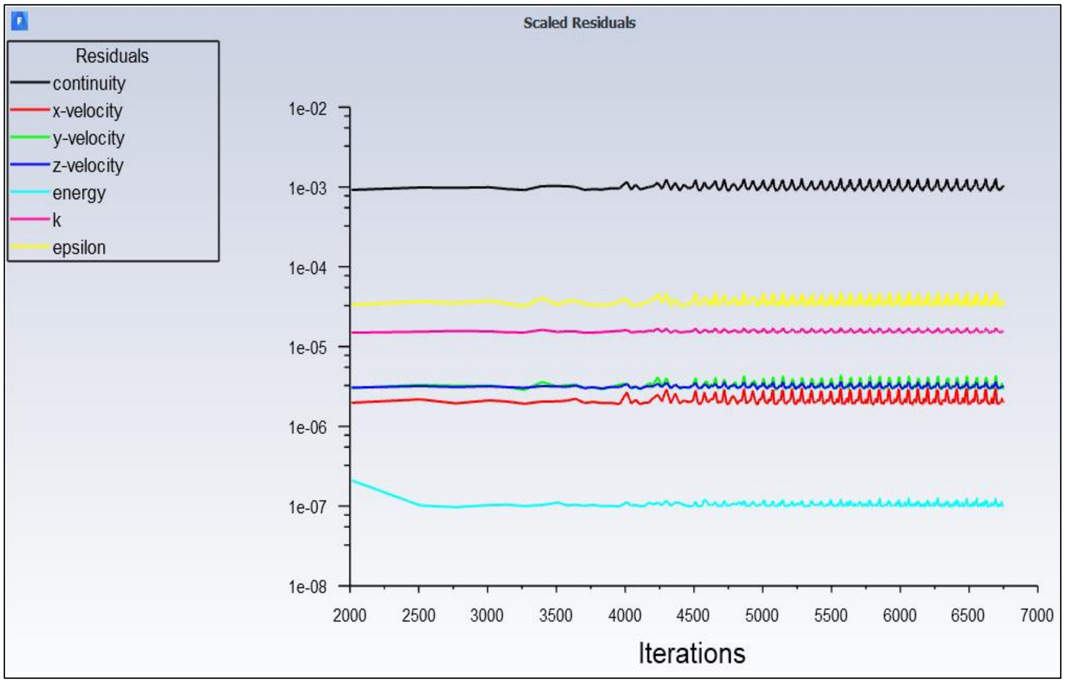

Fig.3.14. Residual convergence plot of 12cm.

In conclusion, this chapter has outlined the simulation procedure using ANSYS Fluent and presented the resulting data. The subsequent chapter will discuss the experimental results and their comparison with the simulation.

Chapter 4: Results and Discussion

Results and Discussion

This chapter comprehensively analyzes the experimental and numerical results of studying the (DPSAC). It encompasses a detailed comparison of the experimental data against the numerical simulations conducted using *ANSYS Fluent*. The validation of the simulation model, through a comparison with empirical results, is aimed at verifying the accuracy and reliability of the computational approach. This chapter also discusses vital findings, explores potential discrepancies, and provides insights into the performance characteristics of the solar collector. The discussion will conclude with implications of the results and suggestions for future research.

4.1. Validation of Numerical Models with Experimental Data

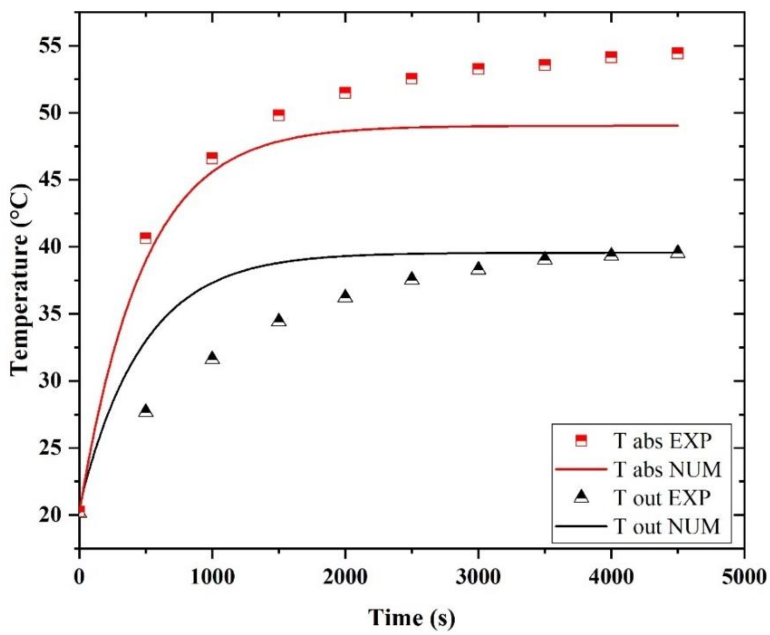

Fig.4.1. Comparison of numerical and experimental temperatures at the outlet and absorber, 3cm configuration.

Fig.4.2. Comparison of numerical and experimental temperatures at the outlet and absorber, 6 cm configuration.

Fig.4.3. Comparison of numerical and experimental temperatures at the outlet and absorber, 9 cm configuration.

Fig.4.4. Comparison of numerical and experimental temperatures at the outlet and absorber, 12 cm configuration.

The average relative error (ARE) is calculated as follows

$$ARE = \frac{1}{N}\sum_{i=1}^{N}\left|\frac{T_{EXPi} - T_{NUMi}}{T_{EXPi}}\right| \times 100\% \qquad (4.1)$$

N : Number of time steps.

Table.4.1. Average relative error by configuration for numerical and experimental data.

4.2. Dynamic Behavior of the DPSAC

Fig.4.5..

Fig.4.6.

Fig.4.7.

Fig.4.8.

4.3. Effect of Depth Flow on the Temporal Thermal Behavior of the DPASC

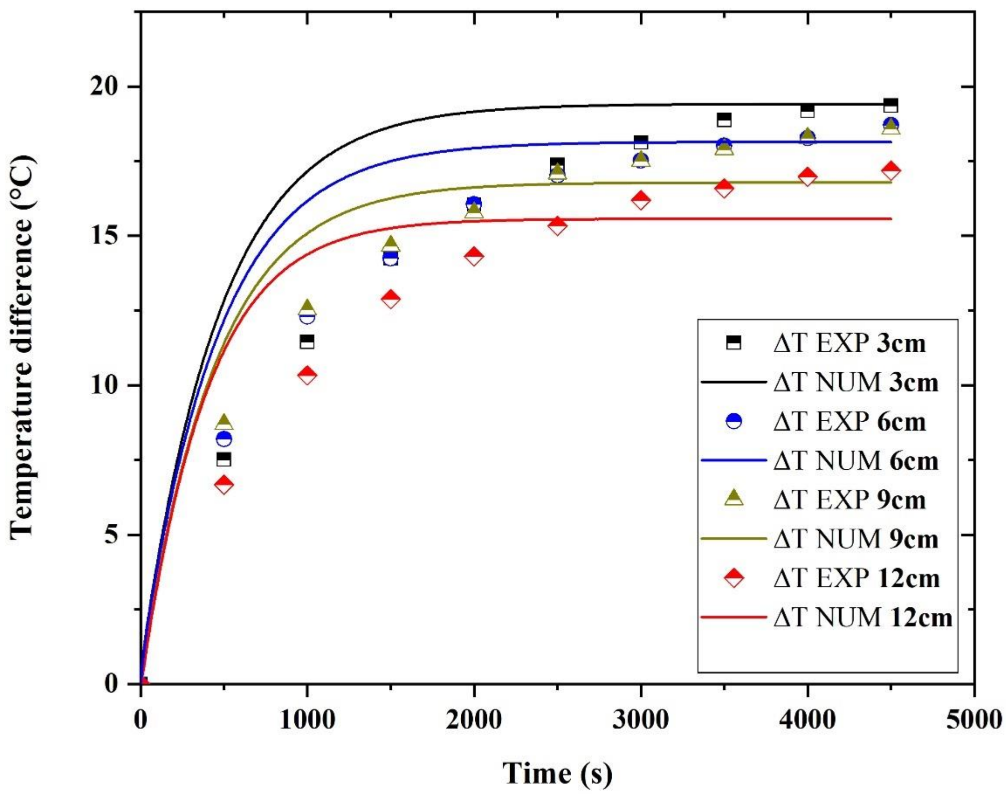

Fig.4.9. Comparison of numerical and experimental temperature gradients for 3 cm, 6 cm, 9 cm, and 12 cm Configurations.

Table. 4.2. Experimental and numerical temperature difference.

4.4. Thermal Efficiency of the DPASC

Table.4.3. Experimental and numerical thermal efficiencies.

General Conclusion

General Conclusion

References

[1] Kumar, A., Singh, A. P., & Singh, O. P. (2020). Efficient designs of double-pass curved solar air heaters. *Renewable Energy, 160*, 1105-1118.

[2] Khanlari, A., Güler, H. Ö., Tuncer, A. D., Şirin, C., Bilge, Y. C., Yılmaz, Y., & Güngör, A. (2020). Experimental and numerical study of the effect of integrating plus-shaped perforated baffles to solar air collector in drying application. *Renewable Energy, 145*, 1677-1692.

[3] Nunes de Oliveira, R., Antonio Rodrigues Filho, F., Pabon, J. J. G., Koury, R. N. N., & Machado, L. (2017). Numerical model of an inflatable solar collector. *Drying Technology, 35*(14), 1733-1741.

[4] Hassan, H., & Abo-Elfadl, S. (2018). Experimental study on the performance of double pass and two inlet ports solar air heater (SAH) at different configurations of the absorber plate. *Renewable Energy, 116*, 728-740.

[5] Salih, M. M. M., Alomar, O. R., Ali, F. A., & Abd, H. M. (2019). An experimental investigation of a double pass solar air heater performance: A comparison between natural and forced air circulation processes. *Solar Energy, 193*, 184-194.

[6] Akrout, O., Ghriss, O., Bouabidi, A., Castellanos, H. G., Mohtarm, S., Keçebaş, A., & Aryanfar, Y. (2024). Investigative analysis of the influence of diverse fin configurations on the performance of a dual pass solar air collector. *Thermal Science and Engineering Progress*, 102545.

[7] Salhi, M., Chaatouf, D., Raillani, B., Bria, A., Amraqui, S., & Mezrhab, A. (2024). Thermal and dynamic improvement of a double pass solar air heater for drying applications. *Thermal Science and Engineering Progress*, 102583.

[8] Korti, A. I. N. (2015). Numerical 3-D heat flow simulations on double-pass solar collector with and without porous media. *Journal of Thermal Engineering, 1*(1), 10-23.

[9] Chávez-Bermúdez, I. A., Rodríguez-Muñoz, N. A., Venegas-Reyes, E., Valenzuela, L., & Ortega-Avila, N. (2022). Thermal performance analysis of a double-pass solar air collector: A CFD approach. *Applied Sciences*, *12*(23), 12199.

[10] Al-Damook, M., Obaid, Z. A. H., Al Qubeissi, M., Dixon-Hardy, D., Cottom, J., & Heggs, P. J. (2019). CFD modeling and performance evaluation of multipass solar air heaters. *Numerical Heat Transfer, Part A: Applications, 76*(6), 438-464.

[11] Omojaro, A. P., & Aldabbagh, L. B. Y. (2010). Experimental performance of single and double pass solar air heater with fins and steel wire mesh as absorber. *Applied Energy, 87*(12), 3759-3765.

[12] Salih, M. M. M., Alomar, O. R., & Yassien, H. N. S. (2021). Impacts of adding porous media on performance of double-pass solar air heater under natural and forced air circulation processes. *International Journal of Mechanical Sciences, 210*, 106738.

[13] Versteeg, H. K., & Malalasekera, W. (No year provided). *An Introduction to Computational Fluid Dynamics*. [Publisher and location needed, otherwise remove from the list if unavailable].

[14] Fatchurrohman, N., & Chia, S. T. (2017, October). Performance of hybrid nano-micro reinforced mg metal matrix composites brake caliper: Simulation approach. In *IOP Conference Series: Materials Science and Engineering* (Vol. 257, No. 1, p. 012060). IOP Publishing.

[15] Yunus, A. C. (2003). *Heat Transfer: A Practical Approach*. McGraw-Hill, New York, p. 210.